Journal of Computational Physics **175,** 168–199 (2002)
doi:10.1006/jcph.2001.6934, available online at http://www.idealibrary.com on IDEAL®

A Space-Time Conservation Element and Solution Element Method for Solving the Two- and Three-Dimensional Unsteady Euler Equations Using Quadrilateral and Hexahedral Meshes

Zeng-Chan Zhang,* S. T. John Yu,* and Sin-Chung Chang†

**Mechanical Engineering Department, Wayne State University, Detroit, Michigan 48202;*
and †NASA Glenn Research Center, Cleveland, Ohio 44135
E-mail: zhangzc@me1.eng.wayne.edu, styu@me1.eng.wayne.edu, and sin-chung.chang@grc.nasa.gov

Received November 21, 2000; revised September 4, 2001

In this paper, we report a version of the space-time conservation element and solution element (CE/SE) method in which the 2D and 3D unsteady Euler equations are simulated using structured or unstructured quadrilateral and hexahedral meshes, respectively. In the present method, mesh values of flow variables and their spatial derivatives are treated as independent unknowns to be solved for. At each mesh point, the value of a flow variable is obtained by imposing a flux conservation condition. On the other hand, the spatial derivatives are evaluated using a finite-difference/weighted-average procedure. Note that the present extension retains many key advantages of the original CE/SE method which uses triangular and tetrahedral meshes, respectively, for its 2D and 3D applications. These advantages include efficient parallel computing, ease of implementing nonreflecting boundary conditions, high-fidelity resolution of shocks and waves, and a genuinely multidimensional formulation without the need to use a dimensional-splitting approach. In particular, because Riemann solvers—the cornerstones of the Godunov-type upwind schemes—are not needed to capture shocks, the computational logic of the present method is considerably simpler. To demonstrate the capability of the present method, numerical results are presented for several benchmark problems including oblique shock reflection, supersonic flow over a wedge, and a 3D detonation flow.

Key Words: the Eular equations; conservation laws; CE/SE method.

0021-9991/02 $35.00

1. INTRODUCTION

The space-time conservation element and solution element (CE/SE) method, originally proposed by Chang and co-workers [1–13], is a new numerical framework for solving conservation laws. The CE/SE method is not an incremental improvement of a previously existing CFD method, and it differs substantially from other well-established methods. The CE/SE method has many nontraditional features, including a unified treatment of space and time, the introduction of conservation element and solution element, and a novel shock-capturing strategy that does not use Riemann solvers. Note that conservation elements are nonoverlapping space-time subdomains introduced such that (i) the computational domain is the union of these subdomains and (ii) flux conservation can be enforced over each of them and also over the union of any combination of them. In contrast, each solution element is a space-time subdomain over which any physical flux vector is approximated using simple smooth functions. In general, a conservation element does not coincide with a solution element.

To date, numerous highly accurate CE/SE steady and unsteady solutions with Mach numbers ranging from 0.0028 to 10 have been obtained without using preconditioning or other special techniques [1–26]. The flow phenomena modeled include traveling and interacting shocks, acoustic waves, shedding vortices, detonation waves, and cavitation. In particular, the rather unique capability of the CE/SE method to resolve both strong shocks and small disturbances (e.g., acoustic waves) simultaneously has been verified through several accurate predictions of experimental data [15–17]. Note that, *while numerical dissipation is required for shock resolution, it may also result in annihilation of small disturbances. Thus a solver that can handle both strong shocks and small disturbances simultaneously must be able to overcome this difficulty*. The design principles of the CE/SE method have been extensively illustrated in the cited references. In this paper, a brief description of the CE/SE method is provided as the background of the present work.

Perhaps one of the most important features of the CE/SE method is the adoption of an integral form of space-time flux conservation as the cornerstone for the subsequent numerical discretization. Note that one derives the conventional finite-volume methods based on Reynolds transport theorem [27], in which space and time are treated separately. As will be shown, this separate treatment of space and time imposes a restriction on the space-time geometry of finite volumes and, as a result, classical Riemann problems arise natually in the course of flux evaluation across an interface. In contrast, because of its unified treatment of space and time, Chang's flux conservation formulation allows a choice of the space-time geometry of CEs that makes it unnecessary to solve Riemann problems. To clarify this fundamental difference, in this Introduction, we first review the conventional integral form for hyperbolic conservation laws in Section 1.1 as a contrast to Chang's integral form, which is described in Section 1.2. The original CE/SE method is reviewed in Section 1.3, and the objectives and outline of the present work are presented in Section 1.4.

1.1. *Conventional Finite-Volume Methods*

Consider the differential form of a conservation law, i.e.,

$$\frac{\partial u}{\partial t} + \underline{\nabla} \cdot \underline{\mathbf{h}} = 0, \tag{1.1}$$

where u is the density of the conserved quantity, $\underline{\mathbf{h}}$ is the spatial flux vector, and $\underline{\nabla}\cdot$ is the spatial divergence operator. Note that, to distingush a spatial object from a space-time object (see below), hereafter the former will be denoted by an underline. By using Reynolds's transport theorem, one can obtain the conventional integral form of Eq. (1.1), i.e.,

$$\frac{\partial}{\partial t}\oint_{\underline{V}} u\,\underline{dv} + \oint_{\underline{S}(\underline{V})} \underline{\mathbf{h}}\cdot\underline{d\mathbf{s}} = 0, \tag{1.2}$$

where $\underline{V}$ is a *fixed spatial domain* (i.e., a "control volume"), $\underline{dv}$ is a spatial volume element, $\underline{S}(\underline{V})$ is the boundary of $\underline{V}$, and $\underline{d\mathbf{s}} = \underline{d\sigma}\,\underline{\mathbf{n}}$ with $\underline{d\sigma}$ and $\underline{\mathbf{n}}$, respectively, being the area and the unit outward normal vector of a surface element on $\underline{S}(\underline{V})$. By integrating Eq. (1.2) over the time interval (t_s, t_f), one obtains

$$\left[\oint_{\underline{V}} u\,\underline{dv}\right]_{t=t_f} - \left[\oint_{\underline{V}} u\,\underline{dv}\right]_{t=t_s} + \int_{t_s}^{t_f} dt \oint_{\underline{S}(\underline{V})} \underline{\mathbf{h}}\cdot\underline{d\mathbf{s}} = 0. \tag{1.3}$$

The discretization of Eq. (1.3) is the focus of conventional finite-volume methods [27].

1.2. *The Space-Time Flux Conservation Formulation*

Let E_N denote an N-dimensional Euclidean space in which $x_1, x_2, \ldots, x_{N-1}$ are spatial coordinates and $x_N = t$, $\nabla\cdot$ be the divergence operator in E_N, and $\mathbf{h} \stackrel{\text{def}}{=} (\underline{\mathbf{h}}, u)$. Then Eq. (1.1) implies $\nabla\cdot\mathbf{h} = 0$. As a result, Gauss's divergence theorem in E_N implies

$$\oint_{S(V)} \mathbf{h}\cdot d\mathbf{s} = 0. \tag{1.4}$$

As depicted in Fig. 1, here $S(V)$ is the boundary of an arbitrary *space-time* region V in E_N and $d\mathbf{s} = d\sigma\,\mathbf{n}$ with $d\sigma$ and $\mathbf{n}$, respectively, being the area and the unit outward normal of a surface element on $S(V)$. Note that: (i) because $\mathbf{h}\cdot d\mathbf{s}$ is the *space-time* flux of $\mathbf{h}$ leaving the

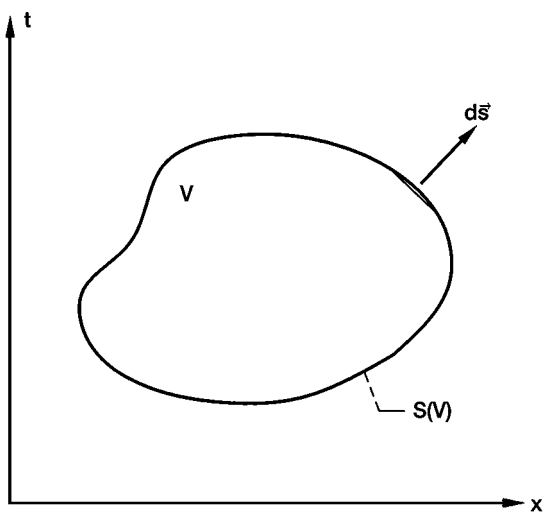

FIG. 1. A surface element on the boundary $S(V)$ of a volume V in a space-time E_2.

region V through the surface element $d\mathbf{s}$, Eq. (1.4) simply states that the total *space-time* flux of $\mathbf{h}$ leaving V through $S(V)$ vanishes; and (ii) all mathematical operations can be carried out as though E_N were an ordinary N-dimensional Euclidean space.

Let $N = 2$. For this case, $x_1 = x$ and $x_2 = t$; $\underline{\mathbf{h}} = h_x$; $\underline{\nabla} \cdot \underline{\mathbf{h}} = \partial h_x / \partial x$; and a "surface element" on $S(V)$ and the "area" of this element reduce to a line segment and the length of this segment, respectively (see Fig. 1). Note that, for an arbitrary V, the spatial projection $\underline{V}(t)$ of the cross section of V at time t generally varies with t. The exception occurs only if V is a cylinder with its axis being parallel to the time axis, such as the rectangle *ABCD* depicted in Fig. 2a. In this case, $\underline{V}(t)$ is independent of t and thus it can be considered as a "control volume."

Let V be the rectangle *ABCD* depicted in Fig. 2a. Then $S(V)$ is formed by the line segments $\overline{AB}$, $\overline{BC}$, $\overline{CD}$, and $\overline{DA}$. Let $t = t_s$ at $\overline{CD}$, $t = t_f$ at $\overline{AB}$, $x = x_s$ at BC, and

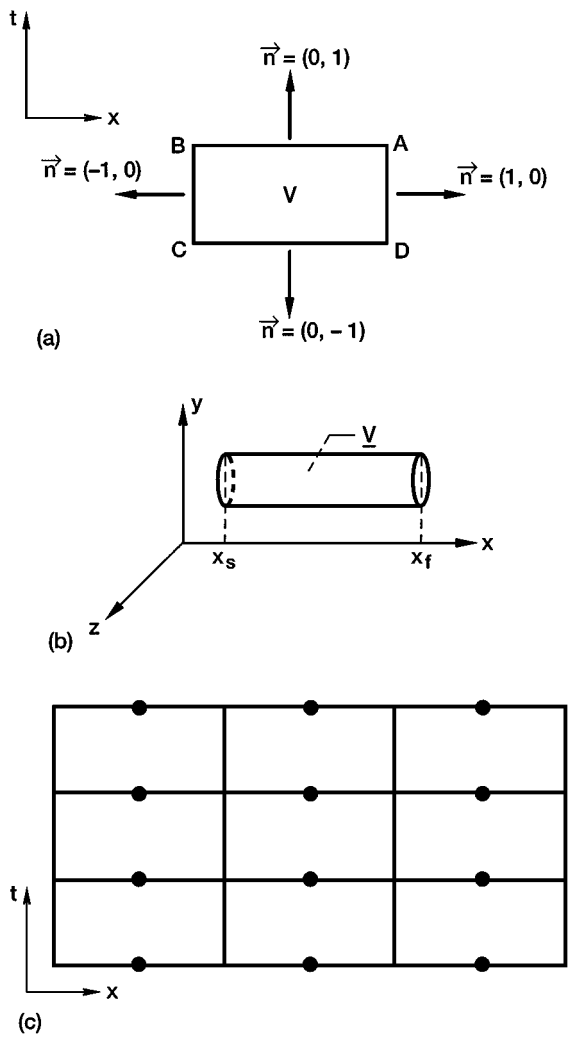

FIG. 2. Space-time geometry of the conventional finite volume method in E_2. (a) A rectangle in E_2. (b) A spatial cylinder aligned in the x direction, (c) A regular space-time mesh.

$x = x_f$ at $\overline{DA}$. Then because $\mathbf{h} = (h_x, u)$, with the aid of Fig. 2a, Eq. (1.4) implies

$$\left[\int_{x_s}^{x_f} u\,dx\right]_{t=t_f} - \left[\int_{x_s}^{x_f} u\,dx\right]_{t=t_s} + \left[\int_{t_s}^{t_f} h_x\,dt\right]_{x=x_f} - \left[\int_{t_s}^{t_f} h_x\,dt\right]_{x=x_s} = 0. \quad (1.5)$$

Note that Eq. (1.3) reduces to Eq. (1.5) for the 1D unsteady case in which $\underline{V}$ is the spatial cylinder of constant cross section depicted in Fig. 2b, $u = u(x, t)$, and $\underline{\mathbf{h}} = (h_x, 0, 0)$ with $h_x = h_x(x, t)$.

Note that generally the discretization of Eq. (1.3) is carried out by dividing the entire space-time computational domain into space-time CEs. Each CE is a cylinder in space-time with its spatial projection being the control volume $\underline{V}$ and its top and bottom faces representing two constant time levels. Because the control volume is a fixed spatial domain, these CEs generally are stacked up exactly on the top of each other; i.e., no staggering of CEs in time is allowed (see Fig. 2c for the $N = 2$ case). With this arrangement of CEs, the vertical interface that separates any two neighboring columns of CEs will always be sandwiched between two neighboring columns of mesh points (marked by dots in Fig. 2c). As such, flux at the vertical interface of two neighboring CEs generally must be evaluated by interpolating the data from the mesh points embedded in these two CEs. Determining how this interpolation should be carried out properly under varying solution behavior is a difficult problem. As will be shown, *with a new space-time arrangement of CEs and mesh points, and a proper definition of SEs, the above difficult interpolation problem can be bypassed completely*.

1.3. *The CE/SE Method*

As an example, the CE/SE method will be described by considering the PDE

$$\frac{\partial u}{\partial t} + \frac{\partial (au)}{\partial x} = 0, \quad (1.6)$$

where a is a constant. Obviously the integral form of Eq. (1.6) is Eq. (1.4) with $N = 2$ and $\mathbf{h} = (au, u)$.

To proceed, let Ψ denote the set of all mesh points in E_2 (dots in Fig. 3a). Each $(j, n) \in \Psi$ is associated with a solution element, i.e., SE(j, n). By definition, SE(j, n) is the interior of the space-time region bounded by a dashed curve depicted in Fig. 3b. It includes a horizontal line segment, a vertical line segment, and their immediate neighborhood.

For any $(x, t) \in$ SE(j, n), $u(x, t)$ and $\mathbf{h}(x, t)$, respectively, are approximated by

$$u^*(x, t; j, n) \stackrel{\text{def}}{=} u_j^n + (u_x)_j^n (x - x_j) + (u_t)_j^n (t - t^n) \quad (1.7)$$

and

$$\mathbf{h}^*(x, t; j, n) \stackrel{\text{def}}{=} (au^*(x, t; j, n), u^*(x, t; j, n)). \quad (1.8)$$

Note that u_j^n, $(u_x)_j^n$, and $(u_t)_j^n$ are constants in SE(j, n); (x_j, t^n) are the coordinates of the mesh point (j, n); and Eq. (1.8) is the numerical analogue of the definition $\mathbf{h} = (au, u)$.

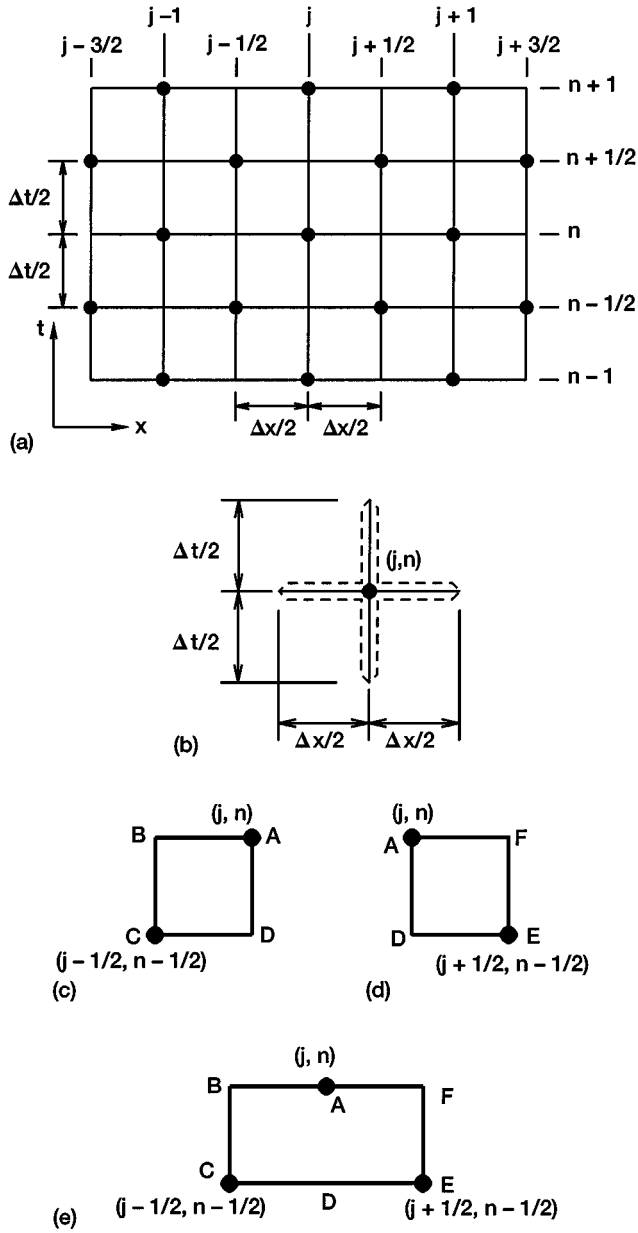

FIG. 3. The SEs and CEs of the a scheme. (a) A staggered space-time mesh. (b) SE(j, n). (c) CE$_-(j, n)$. (d) CE$_+(j, n)$. (e) CE(j, n).

Let $u = u^*(x, t; j, n)$ satisfy Eq. (1.6) within SE(j, n). Then one has $(u_t)_j^n = -a(u_x)_j^n$. As a result, Eq. (1.7) reduces to

$$u^*(x, t; j, n) = u_j^n + (u_x)_j^n[(x - x_j) - a(t - t^n)], \quad (x, t) \in \text{SE}(j, n); \tag{1.9}$$

i.e., u_j^n and $(u_x)_j^n$ are the only independent marching variables associated with (j, n).

Let E_2 be divided into nonoverlapping rectangular regions (see Fig. 3a) referred to as conservation elements. As depicted in Figs. 3c and 3d, two CEs, i.e., CE$_-(j, n)$ and

$\mathrm{CE}_+(j,n)$, are associated with each interior mesh point $(j,n) \in \Psi$. These CEs will be referred to as *basic conservation elements* (BCEs). Contrarily, $\mathrm{CE}(j,n)$ (see Fig. 3e), which is the union of $\mathrm{CE}_-(j,n)$ and $\mathrm{CE}_+(j,n)$, will be referred to as a compounded conservation element (CCE).

Note that, among the line segments forming the boundary of $\mathrm{CE}_-(j,n)$, $\overline{AB}$ and $\overline{AD}$ belong to $\mathrm{SE}(j,n)$, while $\overline{CB}$ and $\overline{CD}$ belong to $\mathrm{SE}(j-1/2, n-1/2)$. Similarly, the boundary of $\mathrm{CE}_+(j,n)$ belongs to either $\mathrm{SE}(j,n)$ or $\mathrm{SE}(j+1/2, n-1/2)$. As a result, by imposing two conservation conditions at each $(j,n) \in \Psi$, i.e.,

$$\oint_{S(CE_\pm(j,n))} \mathbf{h}^* \cdot d\mathbf{s} = 0, \quad (j,n) \in \Psi, \tag{1.10}$$

and using Eqs. (1.8) and (1.9), one has (i)

$$u_j^n = \frac{1}{2}\Big\{(1+\nu)u_{j-1/2}^{n-1/2} + (1-\nu)u_{j+1/2}^{n-1/2} + (1-\nu^2)\Big[(u_x^+)_{j-1/2}^{n-1/2} - (u_x^+)_{j+1/2}^{n-1/2}\Big]\Big\} \tag{1.11}$$

and, assuming $1-\nu^2 \neq 0$, (ii)

$$(u_x^+)_j^n = \frac{1}{2}\Big[u_{j+1/2}^{n-1/2} - u_{j-1/2}^{n-1/2} - (1-\nu)(u_x^+)_{j-1/2}^{n-1/2} - (1+\nu)(u_x^+)_{j+1/2}^{n-1/2}\Big]. \tag{1.12}$$

Here $\nu \overset{\text{def}}{=} a\Delta t/\Delta x$ and $(u_x^+)_j^n \overset{\text{def}}{=} (\Delta x/4)(u_x)_j^n$. The a scheme [1, 5, 8], the explicit nondissipative CE/SE solver for Eq. (1.6), is formed by Eqs. (1.11) and (1.12).

According to Eq. (1.10), the total flux of $\mathbf{h}^*$ leaving the boundary of any BCE is zero. Because the surface integration over any interface separating two neighboring BCEs is evaluated using the information from a single SE, obviously the local conservation relation Eq. (1.10) leads to a global flux conservation relation; i.e., *the total flux of* $\mathbf{h}^*$ *leaving the boundary of any space-time region that is the union of any combination of BCEs will also vanish*. In particular, because $\mathrm{CE}(j,n)$ is the union of $\mathrm{CE}_-(j,n)$ and $\mathrm{CE}_+(j,n)$,

$$\oint_{S(CE(j,n))} \mathbf{h}^* \cdot d\mathbf{s} = 0, \quad (j,n) \in \Psi, \tag{1.13}$$

must follow from Eq. (1.10). In fact, *it can be shown that Eq. (1.13) is equivalent to Eq. (1.11)*.

In addition to the nondissipative a scheme, there is a broad family of dissipative CE/SE solvers of Eq. (1.6) in which only the less stringent conservation condition Eq. (1.13) is assumed [2, 3, 5, 8]. Because Eq. (1.13) is equivalent to Eq. (1.11), for each of these schemes, u_j^n is still evaluated using Eq. (1.11) while $(u_x^+)_j^n$ is evaluated using an equation different from Eq. (1.12). Among these schemes is one (referred to as the a–α scheme) which is among the simplest and yet capable of handling solutions with discontinuities. For this scheme, $(u_x^+)_j^n$ is evaluated using a finite-difference/weighted-average procedure which involves a parameter α (see Eqs. (2.62), (2.63), and (2.65) in [12]). The key disadvantage of the a–α scheme and its extensions (see below) is that, compared with the more general CE/SE schemes, they allow for less freedom in adjusting numerical dissipation. As explained in Section 5.5 of [9], this inflexibility may impose a constraint on the performance of these schemes in numerical simulations involving highly nonuniform meshes.

The above description of the CE/SE development is based on a simple PDE. However, it represents the essence of the general CE/SE development which may involve a system of conservation laws in one, two, or three spatial dimensions. In particular, note that:

(a) The 1D Euler extension of the a–α scheme, which first appears in [2], has been shown to be an accurate and robust shock-capturing solver [2, 3, 5, 6].

(b) In the original 2D extension of the CE/SE method [4, 6–10], triangles are used as the basic building blocks of the spatial meshes. Corresponding to the three sides of a triangle, three BCEs are defined for each mesh point. The union of the three BCEs at a mesh point is the CCE at the same mesh point. Among the family of 2D CE/SE schemes described in [4, 6–10], the 2D a scheme, which has three unknowns u, u_x, and u_y at each mesh point, are constructed by imposing three conservation conditions over the three BCEs at each mesh point. In contrast, only one conservation condition (imposed over the CCE) per mesh point and per conservation law is used in the construction of the 2D Euler a–α scheme (i.e., the scheme defined by Eqs. (6.54), (6.107), and (6.108) in [8]). Because of its simplicity, accuracy, and roubustness, all the numerical results presented in [4, 8, 9] are generated using the 2D Euler a–α scheme.

(c) The 3D Euler a–α scheme [11] is a straightforward extension of the 2D Euler a–α scheme taking into account that: (i) tetrahedrons are used as the basic building blocks of 3D spatial meshes; and (ii) corresponding to the four sides of a tetrahedron, the CCE at each mesh point is the union of the four BCEs defined at the same mesh point.

1.4. *The Objectives and Outline of the Present Work*

In this paper, the 2D and 3D unstructured-mesh a–α Euler schemes are constructed using quadrilateral and hexahedral meshes, respectively. It is shown that the present schemes are also simple, robust, and accurate. The rest of the paper is organized as follows. The 2D and 3D solvers along with their key properties are described in Sections 2 and 3, respectively. Numerical examples are presented in Section 4 to demonstrate the capabilities of the present solvers. The concept of local and global flux conservation for the present 2D scheme with an unstructured mesh along with a post-marching procedure for handling a possible "solution decoupling" problem is discussed in the Appendix. Concluding remarks are given in Section 5.

2. THE 2D UNSTEADY EULER SOLVER

Consider the standard conservation form of the two-dimensional unsteady Euler equations of a perfect gas [9],

$$\frac{\partial u_m}{\partial t} + \frac{\partial f_m}{\partial x} + \frac{\partial g_m}{\partial y} = 0, \quad m = 1, 2, 3, 4, \tag{2.1}$$

where f_m and g_m, $m = 1, 2, 3, 4$, are explicit functions of the independent flow variables u_m, $m = 1, 2, 3, 4$ [9]. Let $x_1 = x$, $x_2 = y$, and $x_3 = t$ be the coordinates of a three-dimensional Euclidean space E_3. Then, in the case that u_m are smooth functions of x, y, z, and t, Eq. (2.1) can be derived from the more fundamental conservation laws

$$\oint_{S(V)} \mathbf{h}_m \cdot d\mathbf{s} = 0, \quad m = 1, 2, 3, 4, \tag{2.2}$$

where $S(V)$ and $d\mathbf{s}$ were defined following Eq. (1.4) and $\mathbf{h}_m \stackrel{\text{def}}{=} (f_m, g_m, u_m)$. Note that Eq. (2.2) is valid even in the presence of flow discontinuities.

For the future development, let

$$f_{m,\ell} \stackrel{\text{def}}{=} \partial f_m/\partial u_\ell, \quad g_{m,\ell} \stackrel{\text{def}}{=} \partial g_m/\partial u_\ell, \quad m, \ell = 1, 2, 3, 4. \tag{2.3}$$

2.1. *Conservation Elements and Solution Elements*

Consider Fig. 4a. Here the x–y plane is divided into nonoverlapping convex quadrilaterals and any two neighboring quadrilaterals share a common side. Moreover, (i) vertices and centroids of quadrilaterals are marked by dots and circles, respectively; (ii) $\underline{Q}$ is the centroid of a typical quadrilateral $\underline{B}_1\underline{B}_2\underline{B}_3\underline{B}_4$; (iii) $\underline{A}_1$, $\underline{A}_2$, $\underline{A}_3$ and $\underline{A}_4$, respectively, are the centroids of the four quadrilaterals neighboring to the quadrilateral $\underline{B}_1\underline{B}_2\underline{B}_3\underline{B}_4$; and (iv) $\underline{Q}^*$ (marked by a cross) is the centroid of the polygon $\underline{A}_1\underline{B}_1\underline{A}_2\underline{B}_2\underline{A}_3\underline{B}_3\underline{A}_4\underline{B}_4$. Hereafter, point $\underline{Q}^*$ (which

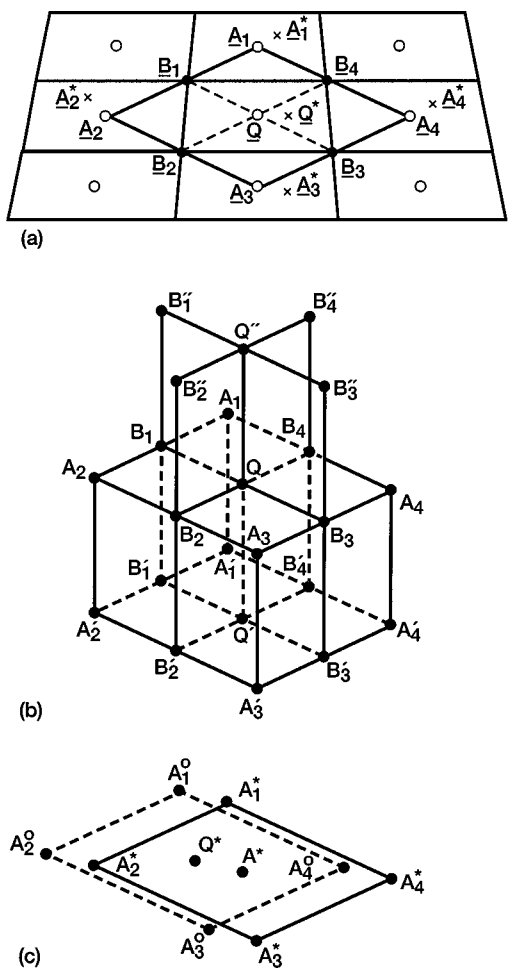

FIG. 4. Space-time geometry of the 2D scheme. (a) Representative grid points in the x–y plane. (b) SEs and CEs. (c) Spatial translation of the quadrilateral $A_1^*A_2^*A_3^*A_4^*$.

generally does not coincide with point $\underline{Q}$) is referred to as the solution point associated with the centroid $\underline{Q}$. Note that points $\underline{A}_1^*$, $\underline{A}_2^*$, $\underline{A}_3^*$, and $\underline{A}_4^*$, which are also marked by crosses, are the solution points associated with the centroids $\underline{A}_1$, $\underline{A}_2$, $\underline{A}_3$, and $\underline{A}_4$, respectively.

Next consider Fig. 4b. Here $t = n\Delta t$ at the nth time level ($n = 0, 1/2, 1, 3/2, \ldots$) and for a given $n > 0$, Q, Q', and Q'', respectively, denote the points on the nth, the $(n-1/2)$th, and the $(n+1/2)$th time levels with point $\underline{Q}$ (see Fig. 4a) being their common spatial projection. Other space-time mesh points, such as those depicted in Fig. 4b, and also those not depicted, are defined similarly. In particular, Q^*, A_1^*, A_2^*, A_3^*, and A_4^*, by definition, lie on the nth time level and, respectively, are the space-time solution mesh points associated with points Q, A_1, A_2, A_3, and A_4, and Q'^*, $A_1'^*$, $A_2'^*$, $A_3'^*$, and $A_4'^*$, by definition, lie on the $(n-1/2)$th time level and, respectively, are the space-time solution mesh points associated with points Q', A_1', A_2', A_3', and A_4'.

With the above preliminaries, the solution element of point Q^*, denoted by $\mathrm{SE}(Q^*)$, is defined as the union of the five plane segments $Q'Q''B_1''B_1'$, $Q'Q''B_2''B_2'$, $Q'Q''B_3''B_3'$, $Q'Q''B_4''B_4'$, and $A_1B_1A_2B_2A_3B_3A_4B_4$ and their immediate neighborhoods. Moreover, the four basic conservation elements (BCEs) of point Q, denoted by $\mathrm{CE}_\ell(Q)$, $\ell = 1, 2, 3, 4$, are defined to be the space-time cylinders $A_1B_1QB_4A_1'B_1'Q'B_4'$, $A_2B_2QB_1A_2'B_2'Q'B_1'$, $A_3B_3QB_2A_3'B_3'Q'B_2'$, and $A_4B_4QB_3A_4'B_4'Q'B_3'$, respectively. In addition, the compounded conservation element of point Q, denoted by $\mathrm{CE}(Q)$, is defined to be the space-time cylinder $A_1B_1A_2B_2A_3B_3A_4B_4A_1'B_1'A_2'B_2'A_3'B_3'A_4'B_4'$, i.e., the union of the above four BCEs.

In this section, the set of the space-time mesh points whose spatial projections are the centroids of quadrilaterals depicted in Fig. 4a is denoted by Ω and the set of the space-time mesh points whose spatial projections are the solution points depicted in Fig. 4a is denoted by Ω^*. Note that the BCEs and the CCE of any mesh point $\in \Omega$ and the SE of any mesh point $\in \Omega^*$ are defined in a manner identical to that described earlier for point Q and Q^*.

2.2. *Approximations within a Solution Element*

For any $Q^* \in \Omega^*$ and any $(x, y, t) \in \mathrm{SE}(Q^*)$, $u_m(x, y, t)$, $f_m(x, y, t)$, $g_m(x, y, t)$, and $\mathbf{h}_m(x, y, t)$, respectively, are approximated by $u_m^*(x, y, t; Q^*)$, $f_m^*(x, y, t; Q^*)$, $g_m^*(x, y, t; Q^*)$, and $\mathbf{h}_m^*(x, y, t; Q^*)$ (see below). For any $m = 1, 2, 3, 4$, let

$$u_m^*(x, y, t; Q^*) \stackrel{\text{def}}{=} (u_m)_{Q^*} + (u_{mx})_{Q^*}(x - x_{Q^*}) + (u_{my})_{Q^*}(y - y_{Q^*}) + (u_{mt})_{Q^*}(t - t^n), \tag{2.4}$$

where (x_{Q^*}, y_{Q^*}, t^n) are the coordinates of the space-time solution mesh point Q^* and $(u_m)_{Q^*}$, $(u_{mx})_{Q^*}$, $(u_{my})_{Q^*}$, and $(u_{mt})_{Q^*}$, which are constants in $\mathrm{SE}(Q^*)$, are the numerical analogues of the values of u_m, $\partial u_m/\partial x$, $\partial u_m/\partial y$, and $\partial u_m/\partial t$ at point Q^*, respectively.

Let $(f_m)_{Q^*}$, $(g_m)_{Q^*}$, $(f_{m,\ell})_{Q^*}$, and $(g_{m,\ell})_{Q^*}$ denote the values of the functions f_m, g_m, $f_{m,\ell}$, and $g_{m,\ell}$, respectively, when u_m, $m = 1, 2, 3, 4$, respectively, assumes the values of $(u_m)_{Q^*}$, $m = 1, 2, 3, 4$. Then, for any m, we define

$$(f_{mx})_{Q^*} \stackrel{\text{def}}{=} \sum_{\ell=1}^{4} (f_{m,\ell})_{Q^*}(u_{\ell x})_{Q^*}, \quad (g_{mx})_{Q^*} \stackrel{\text{def}}{=} \sum_{\ell=1}^{4} (g_{m,\ell})_{Q^*}(u_{\ell x})_{Q^*}, \tag{2.5a}$$

$$(f_{my})_{Q^*} \stackrel{\text{def}}{=} \sum_{\ell=1}^{4} (f_{m,\ell})_{Q^*}(u_{\ell y})_{Q^*}, \quad (g_{my})_{Q^*} \stackrel{\text{def}}{=} \sum_{\ell=1}^{4} (g_{m,\ell})_{Q^*}(u_{\ell y})_{Q^*}, \tag{2.5b}$$

$$(f_{mt})_{Q^*} \stackrel{\text{def}}{=} \sum_{\ell=1}^{4} (f_{m,\ell})_{Q^*} (u_{\ell t})_{Q^*}, \quad (g_{mt})_{Q^*} \stackrel{\text{def}}{=} \sum_{\ell=1}^{4} (g_{m,\ell})_{Q^*} (u_{\ell t})_{Q^*}. \tag{2.5c}$$

Because

$$\frac{\partial f_m}{\partial x} = \sum_{\ell=1}^{4} f_{m,\ell} \frac{\partial u_\ell}{\partial x} \tag{2.6}$$

and because the expression on the right side of the first equation in Eq. (2.5a) is the numerical analogue of that on the right side of Eq. (2.6) at point Q^*, $(f_{mx})_{Q^*}$ can be considered as the numerical analogue of the value of $\partial f_m/\partial x$ at point Q^*. Similarly, $(g_{mx})_{Q^*}$, $(f_{my})_{Q^*}$, $(g_{my})_{Q^*}$, $(f_{mt})_{Q^*}$, and $(g_{mt})_{Q^*}$ can be considered as the numerical analogues of the values of $\partial g_m/\partial x$, $\partial f_m/\partial y$, $\partial g_m/\partial y$, $\partial f_m/\partial t$, and $\partial g_m/\partial t$ at point Q^*, respectively. As a result, for any $m = 1, 2, 3, 4$, we define

$$f_m^*(x, y, t; Q^*) \stackrel{\text{def}}{=} (f_m)_{Q^*} + (f_{mx})_{Q^*}(x - x_{Q^*}) + (f_{my})_{Q^*}(y - y_{Q^*}) + (f_{mt})_{Q^*}(t - t^n) \tag{2.7}$$

and

$$g_m^*(x, y, t; Q^*) \stackrel{\text{def}}{=} (g_m)_{Q^*} + (g_{mx})_{Q^*}(x - x_{Q^*}) + (g_{my})_{Q^*}(y - y_{Q^*}) + (g_{mt})_{Q^*}(t - t^n). \tag{2.8}$$

Also, as an analogue to $\mathbf{h}_m \stackrel{\text{def}}{=} (f_m, g_m, u_m)$, for any $m = 1, 2, 3, 4$, we define

$$\mathbf{h}_m^*(x, y, t; Q^*) \stackrel{\text{def}}{=} (f_m^*(x, y, t; Q^*), g_m^*(x, y, t; Q^*), u_m^*(x, y, t; Q^*)). \tag{2.9}$$

Note that, by their definitions: (i) $(f_m)_{Q^*}$, $(g_m)_{Q^*}$, $(f_{m,\ell})_{Q^*}$, and $(g_{m,\ell})_{Q^*}$ are functions of $(u_m)_{Q^*}$, $m = 1, 2, 3, 4$; (ii) $(f_{mx})_{Q^*}$ and $(g_{mx})_{Q^*}$ are functions of $(u_m)_{Q^*}$ and $(u_{mx})_{Q^*}$, $m = 1, 2, 3, 4$; (iii) $(f_{my})_{Q^*}$ and $(g_{my})_{Q^*}$ are functions of $(u_m)_{Q^*}$ and $(u_{my})_{Q^*}$, $m = 1, 2, 3, 4$; and (iv) $(f_{mt})_{Q^*}$ and $(g_{mt})_{Q^*}$ are functions of $(u_m)_{Q^*}$ and $(u_{mt})_{Q^*}$, $m = 1, 2, 3, 4$.

To proceed, we also assume that, for any $(x, y, t) \in \mathrm{SE}(Q^*)$, and any $m = 1, 2, 3, 4$,

$$\frac{\partial u_m^*(x, y, t; Q^*)}{\partial t} + \frac{\partial f_m^*(x, y, t; Q^*)}{\partial x} + \frac{\partial g_m^*(x, y, t; Q^*)}{\partial y} = 0. \tag{2.10}$$

Note that Eq. (2.10) is the numerical analogue of Eq. (2.1). With the aid of Eqs. (2.4), (2.7), (2.8), (2.5a), and (2.5b), Eq. (2.10) implies that, for any $m = 1, 2, 3, 4$,

$$(u_{mt})_{Q^*} = -(f_{mx})_{Q^*} - (g_{my})_{Q^*} = -\sum_{\ell=1}^{4} [(f_{m,\ell})_{Q^*}(u_{\ell x})_{Q^*} + (g_{m,\ell})_{Q^*}(u_{\ell y})_{Q^*}]. \tag{2.11}$$

Thus $(u_{mt})_{Q^*}$ is a function of $(u_m)_{Q^*}$, $(u_{mx})_{Q^*}$, and $(u_{my})_{Q^*}$, $m = 1, 2, 3, 4$. From this result and the facts stated following Eq. (2.9), one concludes that *the only independent discrete solution variables associated with the space-time solution point* Q^* *are* $(u_m)_{Q^*}$, $(u_{mx})_{Q^*}$, *and* $(u_{my})_{Q^*}$, $m = 1, 2, 3, 4$.

2.3. *Evaluation of* $(u_m)_{Q^*}$

Based on Figs. 4a and 4b, we introduce the following preliminaries:

(a) The boundary of CE(Q) belongs to the union of SE(Q^*) and SE($A_\ell'^*$), $\ell = 1, 2, 3, 4$. Specifically, (i) the octagon $A_1B_1A_2B_2A_3B_3A_4B_4$ belongs to SE(Q^*); (ii) the quadrilaterals $A_1'B_1'Q'B_4'$, $A_1'B_4'B_4A_1$, and $A_1'B_1'B_1A_1$ belong to SE($A_1'^*$); (iii) the quadrilaterals $A_2'B_2'Q'B_1'$, $A_2'B_1'B_1A_2$, and $A_2'B_2'B_2A_2$ belong to SE($A_2'^*$); (iv) the quadrilaterals $A_3'B_3'Q'B_2'$, $A_3'B_2'B_2A_3$, and $A_3'B_3'B_3A_3$ belong to SE($A_3'^*$); and (v) the quadrilaterals $A_4'B_4'Q'B_3'$, $A_4'B_3'B_3A_4$, and $A_4'B_4'B_4A_4$ belong to SE($A_4'^*$). Note that, by definition, (i) the quadrilaterals $A_1B_1QB_4$, $A_2B_2QB_1$, $A_3B_3QB_2$, and $A_4B_4QB_3$, which form the octagon $A_1B_1A_2B_2A_3B_3A_4B_4$ (the top face of CE(Q)), also belong to SE(A_1^*), SE(A_2^*), SE(A_3^*), and SE(A_4^*), respectively; and (ii) the octagon $A_1'B_1'A_2'B_2'A_3'B_3'A_4'B_4'$ (the bottom face of the CE(Q)) also belongs to SE(Q'^*). However, in the evaluation of Eq. (2.13) (see below), by assumption, the top face of CE(Q) is considered to be a subset of SE(Q^*) while the bottom face is considered to be the union of subsets of SE($A_\ell'^*$), $\ell = 1, 2, 3, 4$.

(b) Let Γ be a space-time plane segment lying within SE(Q^*). Let A be the area of Γ, (x_c, y_c, t_c) be the coordinates of the centroid of Γ, and $\mathbf{n}$ be a unit vector normal to Γ. Then, because $u_m^*(x, y, t; Q^*)$, $f_m^*(x, y, t; Q^*)$, and $g_m^*(x, y, t; Q^*)$ are linear in x, y, and t, Eq. (2.9) implies that

$$\int_\Gamma \mathbf{h}_m^* \cdot d\mathbf{s} = \mathbf{h}_m^*(x_c, y_c, t_c; Q^*) \cdot A\mathbf{n}, \tag{2.12}$$

where $d\mathbf{s} = d\sigma\, \mathbf{n}$ with $d\sigma$ being the area of a surface element on Γ.

(c) Let S denote the area of the top face $A_1B_1A_2B_2A_3B_3A_4B_4$ of CE(Q). Because the unit outward normal vector (outward from the interior of CE(Q)) of this face is $(0, 0, 1)$, its surface vector (i.e., the unit outward normal vector multiplied by the area) is $(0, 0, S)$.

(d) Let (x^ℓ, y^ℓ), $\ell = 1, 2, 3, 4$, denote the spatial coordinates of the centroids of the quadrilaterals $A_1'B_1'Q'B_4'$, $A_2'B_2'Q'B_1'$, $A_3'B_3'Q'B_2'$, and $A_4'B_4'Q'B_3'$, respectively, and let S^ℓ, $\ell = 1, 2, 3, 4$, denote the areas of the above four quadrilaterals, respectively. Then $(x^\ell, y^\ell, t^{n-1/2})$, $\ell = 1, 2, 3, 4$, are the coordinates of the above four centroids, respectively, and $(0, 0, -S^\ell)$, $\ell = 1, 2, 3, 4$, are the surface vectors of the above four quadrilaterals, respectively. Furthermore, because the above four quadrilaterals form the bottom face of CE(Q) and because the area of the top face of CE(Q) is identical to that of the bottom face, one concludes that $S = \sum_{\ell=1}^4 S^\ell$.

(e) Let the eight side faces $A_1'B_4'B_4A_1$, $A_1'B_1'B_1A_1$, $A_2'B_1'B_1A_2$, $A_2'B_2'B_2A_2$, $A_3'B_2'B_2A_3$, $A_3'B_3'B_3A_3$, $A_4'B_3'B_3A_4$, and $A_4'B_4'B_4A_4$ of CE(Q) be assigned the indices $(1, 1)$, $(2, 1)$, $(1, 2)$, $(2, 2)$, $(1, 3)$, $(2, 3)$, $(1, 4)$, and $(2, 4)$, respectively. Hereafter each side face with the indices (k, ℓ) is referred to as the (k, ℓ) side face. For each ℓ, by definition, the $(1, \ell)$ and $(2, \ell)$ side faces belong to SE($A_\ell'^*$). Because the spatial projection of each side face is a line segment on the x–y plane and because each side face is sandwiched between the $(n - 1/2)$th and the nth time levels, one concludes that, for the (k, ℓ) side face, its surface vector and the coordinates of its centroid, respectively, are given by $(\Delta t/2)\lambda_k^\ell(n_{kx}^\ell, n_{ky}^\ell, 0)$ and $(x_k^\ell, y_k^\ell, t^n - \Delta t/4)$. Here λ_k^ℓ, $(n_{kx}^\ell, n_{ky}^\ell)$, and (x_k^ℓ, y_k^ℓ), respectively, denote the length, the unit outward normal (on the x–y plane), and the coordinates of the midpoint of the spatial projection of the (k, ℓ) side face.

(f) Note that: (i) (x_{Q^*}, y_{Q^*}, t^n) are the coordinates of the centroid Q^* of the top face $A_1B_1A_2B_2A_3B_3A_4B_4$ of CE(Q); (ii) $u_m^*(x_{Q^*}, y_{Q^*}, t^n; Q^*) = (u_m)_{Q^*}$ (see Eq. (2.4)); and

(iii) the surface vector of the top face is $(0, 0, S)$. As a result, Eqs. (2.9) and (2.12) imply that the flux of $\mathbf{h}_m^*$ leaving CE(Q) through its top face is $(u_m)_{Q^*}S$. Similarly, by using the information presented in items (a), (b), (d), and (e), the flux of $\mathbf{h}_m^*$ leaving the other faces of CE(Q) can be evaluated in terms of the independent marching variables at points $A_\ell'^*$, $\ell = 1, 2, 3, 4$.

Let

$$\oint_{S(CE(Q))} \mathbf{h}_m^* \cdot d\mathbf{s} = 0, \quad m = 1, 2, 3, 4, \tag{2.13}$$

i.e., the total flux of $\mathbf{h}_m^*$ leaving CE(Q) through its boundary vanishes. Then, with the aid of the above preliminaries, it can be shown that

$$(u_m)_{Q^*} = \left(\sum_{\ell=1}^{4} R_m^\ell \right) \Big/ S, \quad m = 1, 2, 3, 4, \tag{2.14}$$

where, for any $m, \ell = 1, 2, 3, 4$,

$$\begin{aligned} R_m^\ell = {} & S^\ell \, u_m^*(x^\ell, y^\ell, t^{n-1/2}; A_\ell'^*) - \sum_{k=1}^{2} \frac{\Delta t}{2} \lambda_k^\ell \big[n_{kx}^\ell \, f_m^*\big(x_k^\ell, y_k^\ell, t^n - \Delta t/4; A_\ell'^*\big) \\ & + n_{ky}^\ell \, g_m^*\big(x_k^\ell, y_k^\ell, t^n - \Delta t/4; A_\ell'^*\big) \big]. \end{aligned} \tag{2.15}$$

Because, by definition, $t = t^{n-1/2}$ for any point $A_\ell'^*$, here the functions $u_m^*(x, y, t; A_\ell'^*)$, $f_m^*(x, y, t; A_\ell'^*)$, and $g_m^*(x, y, t; A_\ell'^*)$ are defined using Eqs. (2.4), (2.7), and (2.8), respectively, with the symbols Q^* and t^n in these equations being replaced by $A_\ell'^*$ and $t^{n-1/2}$, respectively. As a result, each R_m^ℓ and therefore each $(u_m)_{Q^*}$, an independent marching variable at the nth time level, is a function of several independent marching variables at the $(n - 1/2)$th time level, i.e., $(u_m)_{A_\ell'^*}$, $(u_{mx})_{A_\ell'^*}$, and $(u_{my})_{A_\ell'^*}$, $m, \ell = 1, 2, 3, 4$.

2.4. *Evaluation of* $(u_{mx})_{Q^*}$ *and* $(u_{my})_{Q^*}$

A finite-difference approach similar to that given in [10] is employed here to evaluate $(u_{mx})_{Q^*}$ and $(u_{my})_{Q^*}$. First, we perform a spatial translation of the quadrilateral $A_1^*A_2^*A_3^*A_4^*$ so that the centroid of the resulting new quadrilateral $A_1^oA_2^oA_3^oA_4^o$ coincides with Q^* (see Fig. 4c). Let the centroid of the quadrilateral $A_1^*A_2^*A_3^*A_4^*$ and its spatial coordinates be denoted by A^* and (x_{A^*}, y_{A^*}), respectively. Then $(x_{A_\ell^o}, y_{A_\ell^o})$, the spatial coordinates of A_ℓ^o, are

$$x_{A_\ell^o} = x_{A_\ell^*} + x_{Q^*} - x_{A^*} \quad \text{and} \quad y_{A_\ell^o} = y_{A_\ell^*} + y_{Q^*} - y_{A^*}, \quad \ell = 1, 2, 3, 4. \tag{2.16}$$

To proceed, let

$$(u_m)_{A_\ell^o} \stackrel{\text{def}}{=} u_m^*\big(x_{A_\ell^o}, y_{A_\ell^o}, t^n; A_\ell'^*\big), \quad m, \ell = 1, 2, 3, 4. \tag{2.17}$$

Next, for any $m = 1, 2, 3, 4$, consider the three points in the x–y–u space with the coordinates $(x_{Q^*}, y_{Q^*}, (u_m)_{Q^*})$, $(x_{A_1^o}, y_{A_1^o}, (u_m)_{A_1^o})$, and $(x_{A_2^o}, y_{A_2^o}, (u_m)_{A_2^o})$, respectively. The values of $\partial u/\partial x$ and $\partial u/\partial y$ on the plane that intercepts the three points are given by

$$\big(u_{mx}^{(1)}\big)_{Q^*} \stackrel{\text{def}}{=} \Delta_x/\Delta \quad \text{and} \quad \big(u_{my}^{(1)}\big)_{Q^*} \stackrel{\text{def}}{=} \Delta_y/\Delta \quad (\Delta \neq 0), \tag{2.18}$$

where

$$\Delta \stackrel{\text{def}}{=} \begin{vmatrix} x_{A_1^o} - x_{Q^*} & y_{A_1^o} - y_{Q^*} \\ x_{A_2^o} - x_{Q^*} & y_{A_2^o} - y_{Q^*} \end{vmatrix}, \tag{2.19a}$$

$$\Delta_x \stackrel{\text{def}}{=} \begin{vmatrix} (u_m)_{A_1^o} - (u_m)_{Q^*} & y_{A_1^o} - y_{Q^*} \\ (u_m)_{A_2^o} - (u_m)_{Q^*} & y_{A_2^o} - y_{Q^*} \end{vmatrix}, \tag{2.19b}$$

and

$$\Delta_y \stackrel{\text{def}}{=} \begin{vmatrix} (u_m)_{A_1^o} - (u_m)_{Q^*} & x_{Q^*} - x_{A_1^o} \\ (u_m)_{A_2^o} - (u_m)_{Q^*} & x_{Q^*} - x_{A_2^o} \end{vmatrix}. \tag{2.19c}$$

Note that: (i) $\Delta = 0$ if and only if the spatial projections of A_1^o, A_2^o and Q^* are collinear; and (ii) similarly, $(u_{mx}^{(k)})_{Q^*}$ and $(u_{my}^{(k)})_{Q^*}$, $k = 2, 3, 4$, are defined, respectively, by replacing the points A_1^o and A_2^o in the above operations with A_2^o and A_3^o, A_3^o and A_4^o, and A_4^o and A_1^o, respectively.

With the above preliminaries, for each $m = 1, 2, 3, 4$, $(u_{mx})_{Q^*}$ and $(u_{my})_{Q^*}$ may be evaluated by

$$(u_{mx})_{Q^*} = \frac{1}{4}\sum_{k=1}^{4} \left(u_{mx}^{(k)}\right)_{Q^*}, \quad (u_{my})_{Q^*} = \frac{1}{4}\sum_{k=1}^{4} \left(u_{my}^{(k)}\right)_{Q^*}. \tag{2.20}$$

Alternatively, for a flow with steep gradients or discontinuities, the simple averages in Eq. (2.20) may be replaced by weighted averages, i.e.,

$$(u_{mx})_{Q^*} = \begin{cases} 0, & \text{if } \theta_{mk} = 0,\ k = 1, 2, 3, 4, \\ \sum_{k=1}^{4} \left[\left(W_m^{(k)}\right)^{\alpha} \left(u_{mx}^{(k)}\right)_{Q^*}\right] \Big/ \sum_{k=1}^{4} \left(W_m^{(k)}\right)^{\alpha}, & \text{otherwise} \end{cases} \tag{2.21a}$$

and

$$(u_{my})_{Q^*} = \begin{cases} 0, & \text{if } \theta_{mk} = 0,\ k = 1, 2, 3, 4, \\ \sum_{k=1}^{4} \left[\left(W_m^{(k)}\right)^{\alpha} \left(u_{my}^{(k)}\right)_{Q^*}\right] \Big/ \sum_{k=1}^{4} \left(W_m^{(k)}\right)^{\alpha}, & \text{otherwise.} \end{cases} \tag{2.21b}$$

Here $\alpha \geq 0$ is an adjustable constant (usually $\alpha = 1$ or $\alpha = 2$),

$$\theta_{mk} \stackrel{\text{def}}{=} \sqrt{\left[\left(u_{mx}^{(k)}\right)_{Q^*}\right]^2 + \left[\left(u_{my}^{(k)}\right)_{Q^*}\right]^2}, \quad m, k = 1, 2, 3, 4, \tag{2.22}$$

and

$$W_m^{(1)} \stackrel{\text{def}}{=} \theta_{m2}\theta_{m3}\theta_{m4}, \quad W_m^{(2)} \stackrel{\text{def}}{=} \theta_{m3}\theta_{m4}\theta_{m1}, \quad W_m^{(3)} \stackrel{\text{def}}{=} \theta_{m4}\theta_{m1}\theta_{m2}, \quad W_m^{(4)} \stackrel{\text{def}}{=} \theta_{m1}\theta_{m2}\theta_{m3}. \tag{2.23}$$

Note that: (i) to avoid dividing by zero, in practice a small positive number such as 10^{-60} is added to the denominators that appear in Eqs. (2.21a) and (2.21b); and (ii) Eqs. (2.21a) and (2.21b) reduce to Eq. (2.20) if $\alpha = 0$.

2.5. *Remarks and Discussion*

The present 2D Euler solver is formed using Eqs. (2.14), (2.21a), and (2.21b). Stability of the solver generally requires that $\alpha \geq 0$ and that the maximal *CFL* number <1. Also, with $\alpha \geq 1$, the solver is capable of suppressing numerical oscillations near a discontinuity, and solutions generated by the solver tend to become more smeared as the *CFL* number decreases or the value of α increases. Other key properties of this solver are given in the following remarks:

(a) The stencil of the present explicit solver is formed by one point at the upper time level and four points at the lower time level. Because the spatial projections of the four points at the lower time level are the immediate neighbors of that of the point at the upper time level, the stencil is staggered in space-time, and it is the most compact among the schemes using quadrilateral meshes. As a result, the solver is ideal for parallel computations.

(b) For a uniform mesh, points such as Q, Q^*, and A^* referred to earlier coincide with one another. In this case, the present solver can be greatly simplified. Also, by using the arguments presented in [8, 9] and also by numerical experiments, it can be shown that the simplified scheme is second order in accuracy.

(c) The present scheme is applicable to both structured and unstructured meshes. For a structured mesh, the set Ω^* may be divided into two disjoint subsets Ω^*_+ and Ω^*_- with the following property: If any point, say point Q^*, belongs to Ω^*_+ (Ω^*_-), then the six space-time solution mesh points immediately neighboring to point Q^*, i.e., points Q'^*, Q''^*, and A^*_ℓ, $\ell = 1, 2, 3, 4$, belong to Ω^*_- (Ω^*_+). Because, for each $\ell = 1, 2, 3, 4$, points A'^*_ℓ and A^*_ℓ are immediate neighbors of each other and thus they must belong to different subsets, one concludes that points Q^* and A'^*_ℓ, $\ell = 1, 2, 3, 4$, which form the stencil of the present marching scheme, belong to the same subset. From the above observations, it is seen that each of Ω^*_+ and Ω^*_- represents a *staggered* space-time mesh. As such, the entire space-time mesh is a dual space-time mesh [9], i.e., the union of two disjoint staggered space-time meshes. Furthermore, it is also obvious that the marching over Ω^*_+ is completely decoupled from that over Ω^*_-, i.e., marching needs to be carried out only over one of these two staggered space-time meshes, unless the decoupling is prevented by other factors such as the boundary conditions imposed. Note that boundary values generally are not updated using the main marching scheme. As a result, solution values of Ω^*_+ and Ω^*_- may become coupled near a boundary (see Section 4).

(d) Consider the decoupling case referred to in item (c). Let a space-time mesh point belong to Ω_+ (Ω_-) if and only if its associated space-time solution mesh point belongs to Ω^*_+ (Ω^*_-). Then it is obvious that the set Ω is formed by the two disjoint sets Ω_+ and Ω_-. Moreover, the CCEs of the mesh points in Ω_+ (Ω_-) do not overlap among themselves and they can fill any domain in E_3. Furthermore, because the surface integration over any interface separating two neighboring and nonoverlapping CCEs is evaluated using the information from the same SE (i.e., the flux leaving a CCE through its interface with a neighboring CCE is the negative of the flux leaving the neighboring CCE through this interface), a summation of the local conservation conditions Eq. (2.13) over the mesh points $Q \in \Omega_+$ (Ω_-) leads to a global conservation condition, i.e., for each $m = 1, 2, 3, 4$, the total flux of $\mathbf{h}^*_m$ leaving the boundary of any space-time region that is the union of any combination of the CCEs associated with Ω_+ (Ω_-) vanishes. Note that a similar discussion for the general case in which decoupling may not occur will be given in the Appendix.

(e) The present solver and the triangular-mesh-based solver described in [10] are constructed using similar techniques. Using these techniques and their trivial extensions, one can easily develop a 2D CE/SE solver for spatial meshes formed by polygons of different shapes. An advantage of using such a mixed mesh is that a geometrically complex spatial subdomain can be filled easily using triangles while a less complex subdomain, such as a near-wall region, can be filled using more regular shaped polygons such as quadrilaterals.

(f) Because of the space-time staggering nature of the stencil of the present scheme, a solution of the present scheme *may* appear as the overlapping of two distinctively different solutions (especially in a high-gradient region) after many marching steps. The significance of this "solution decoupling" problem and how to handle it are discussed in the Appendix. Note that this problem could occur even in the absence of a complete of Ω_+^* and Ω_-^* decoupling referred to earlier. Also, because the solution decoupling problem is not significant for the test problems discussed in Section 4, the numerical results presented there are generated without using the post-marching procedure described in the Appendix.

3. THE 3D UNSTEADY EULER SOLVER

For the current 3D case, Eqs. (2.1)–(2.3) are replaced by

$$\frac{\partial u_m}{\partial t} + \frac{\partial f_m}{\partial x} + \frac{\partial g_m}{\partial y} + \frac{\partial q_m}{\partial z} = 0, \quad m = 1, 2, 3, 4, 5, \tag{3.1}$$

$$\oint_{S(V)} \mathbf{h}_m \cdot d\mathbf{s} = 0, \quad m = 1, 2, 3, 4, 5, \tag{3.2}$$

and

$$f_{m,\ell} \stackrel{\text{def}}{=} \partial f_m / \partial u_\ell, \quad g_{m,\ell} \stackrel{\text{def}}{=} \partial g_m / \partial u_\ell, \quad q_{m,\ell} \stackrel{\text{def}}{=} \partial q_m / \partial u_\ell, \quad m, \ell = 1, 2, 3, 4, 5, \tag{3.3}$$

respectively. Here $\mathbf{h}_m \stackrel{\text{def}}{=} (f_m, g_m, q_m, u_m)$ and the three-dimensional Euclidean space E_3 referred to in Section 2 is replaced by the four-dimensional Euclidean space E_4 with $x_1 = x$, $x_2 = y$, $x_3 = z$, and $x_4 = t$.

3.1. *Conservation Elements and Solution Elements*

The spatial computational domain is divided into nonoverlapping convex hexahedrons of arbitrary shape with the understanding that any two neighboring hexahedrons share a common face. In Fig. 5, $\underline{Q}$ (marked by a circle) is the centroid of a typical hexahedron $\underline{B}_1\underline{B}_2\underline{B}_3\underline{B}_4\underline{B}_5\underline{B}_6\underline{B}_7\underline{B}_8$ (hereafter referred to as the central hexahedron). Each of the central hexahedron's six neighboring hexahedrons is arbitrarily assigned an identification index $\ell = 1, 2, \ldots, 6$, i.e., the neighboring hexahedron with the index ℓ is referred to as the ℓth neighbor of the central hexahedron. Also, the centroid of the ℓth neighbor will be denoted by $\underline{A}_\ell$. As an example, the central hexahedron and its first neighbor is separated by the quadrilateral $\underline{B}_1\underline{B}_4\underline{B}_8\underline{B}_5$ in Fig. 5.

With the above preliminaries, we proceed with the following definitions:

(a) Point $\underline{Q}$ and the two end points (say points $\underline{B}_1$ and $\underline{B}_2$) of any of the twelve edges of the central hexahedron form a triangle. Each of the twelve triangles so formed is arbitrarily assigned an index $j = 1, 2, 3, \ldots, 12$ and denoted by $\Delta(j)$.

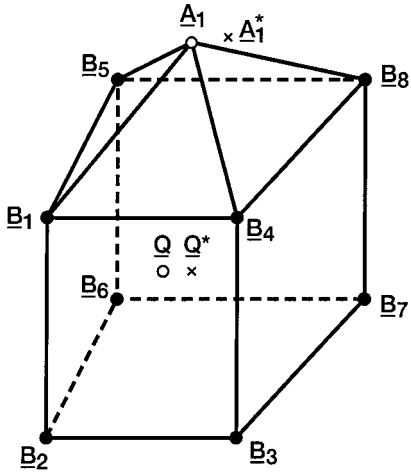

FIG. 5. Representative grid points in the x–y–z space.

(b) Given any $\ell = 1, 2, \ldots, 6$, a triangle is formed by the point $\underline{A}_\ell$ and the two end points of any of the four edges of the interface (a quadrilateral) that separates the central hexahedron and its ℓth neighbor. Each of the four triangles so formed with the same ℓ is arbitrarily assigned an index $k = 1, 2, 3, 4$, and denoted by $\Delta(k, \ell)$. As an example, $\Delta\underline{A}_1\underline{B}_1\underline{B}_4$, $\Delta\underline{A}_1\underline{B}_4\underline{B}_8$, $\Delta\underline{A}_1\underline{B}_8\underline{B}_5$, and $\Delta\underline{A}_1\underline{B}_5\underline{B}_1$ depicted in Fig. 5 have the same $\ell = 1$. Therefore they may be denoted by $\Delta(1, 1)$, $\Delta(2, 1)$, $\Delta(3, 1)$, and $\Delta(4, 1)$, respectively.

(c) The centroid of the 24-faced polyhedron $\underline{B}_1\underline{B}_2\underline{B}_3\underline{B}_4\underline{B}_5\underline{B}_6\underline{B}_7\underline{B}_8\underline{A}_1\underline{A}_2\underline{A}_3\underline{A}_4\underline{A}_5\underline{A}_6$ is referred to as the solution point associated with point $\underline{Q}$. Note that the above 24-faced polyhedron hereafter is denoted by $\underline{V}(24)$ and the centroid of $\underline{V}(24)$ is denoted by $\underline{Q}^*$ and marked by a cross in Fig. 5.

(d) Given any $\ell = 1, 2, \ldots, 6$, points $\underline{Q}$ and $\underline{A}_\ell$ and the four vertices of the quadrilateral interface that separates the central hexahedron and its ℓth neighbor are the vertices of a octahedron. This octahedron hereafter is denoted by $\underline{V}(8; \ell)$.

In the space-time computational domain, again we assume that $t = n\Delta t$ at the nth time level ($n = 0, 1/2, 1, 3/2, \ldots$). Also, for a given $n > 0$, let Q, Q', and Q'' (not shown), respectively, be the points on the nth, $(n - 1/2)$th, and $(n + 1/2)$th time levels with point $\underline{Q}$ being their common spatial projection. Other space-time mesh points such as (i) Q^* and $\overline{Q^*}$; (ii) B_k, B'_k, and B''_k, $k = 1, 2, 3, 4, 5, 6, 7, 8$; and (iii) A_ℓ, A^*_ℓ, A'_ℓ, and A'^*_ℓ, $\ell = 1, 2, \ldots, 6$, are defined similarly. Because geometric objects in E_4 generally are difficult to visualize, they will be described analytically in the following discussions.

To proceed, note that a "plane" (termed a hyperplane) in E_4, by definition, is a subspace of E_4 defined by a linear equation i.e.,

$$a_1x + a_2y + a_3z + a_4t = a_0, \quad ((a_1)^2 + (a_2)^2 + (a_3)^2 + (a_4)^2 \neq 0), \tag{3.4}$$

where a_k, $k = 0, 1, 2, 3, 4$, are constants. As a result, a hyperplane in E_4 is a three-dimensional subspace. The unit normal to the hyperplane is

$$\mathbf{n} = \pm\frac{(a_1, a_2, a_3, a_4)}{\sqrt{(a_1)^2 + (a_2)^2 + (a_3)^2 + (a_4)^2}}. \tag{3.5}$$

Note that a hyperplane segment, by definition, is a bounded region of a hyperplane.

Two types of hyperplane segments in E_4 are involved in the definition of SEs to be given shortly. A hyperplane segment of type I, denoted by $\Gamma(\underline{V}; t_c)$, is formed by all the points (x, y, z, t) that satisfy the conditions $t = t_c$ and $(x, y, z) \in \underline{V}$, where t_c is a constant and $\underline{V}$ denotes a 3D spatial region. Obviously, the equation $t = t_c$ is a special form of Eq. (3.4). Also, it can be shown that:

(a) The unit normal to $\Gamma(\underline{V}; t_c)$ is $(0, 0, 0, \pm 1)$.
(b) The "area" of $\Gamma(\underline{V}; t_c)$ is the volume of $\underline{V}$.
(c) The coordinates of the centroid of $\Gamma(\underline{V}; t_c)$ are (x_c, y_c, z_c, t_c), where (x_c, y_c, z_c) are the coordinates of the centroid of $\underline{V}$.

In contrast, a hyperplane segment of type II, denoted by $\Gamma(\underline{S}; t_-, t_+)$, is formed by all the points (x, y, z, t) that satisfy the conditions $(x, y, z) \in \underline{S}$ and $t_- \le t \le t_+$, where $\underline{S}$ denotes a spatial plane segment and t_- and t_+ $(t_- < t_+)$ are constants. Note that every point (x, y, z) on the spatial plane segment $\underline{S}$ satisfies a linear equation of the form

$$c_1 x + c_2 y + c_3 z = c_0, \quad ((c_1)^2 + (c_2)^2 + (c_3)^2 \neq 0), \tag{3.6}$$

where c_k, $k = 0, 1, 2, 3$, are constants. Thus every point (x, y, z, t) on $\Gamma(\underline{S}; t_-, t_+)$ also satisfies a special form of Eq. (3.4), i.e., Eq. (3.6). Moreover, it can be shown that:

(a) The unit normal to $\Gamma(\underline{S}; t_-, t_+)$ is $(\underline{\mathbf{n}}, 0)$, where $\underline{\mathbf{n}}$ is the unit normal to the spatial plane segment $\underline{S}$, i.e.,

$$\underline{\mathbf{n}} = \pm \frac{(c_1, c_2, c_3)}{\sqrt{(c_1)^2 + (c_2)^2 + (c_3)^2}}. \tag{3.7}$$

(b) The "area" of $\Gamma(\underline{S}; t_-, t_+)$ is the area of $\underline{S}$ multiplied by $(t_+ - t_-)$.
(c) The coordinates of the centroid of $\Gamma(\underline{S}; t_-, t_+)$ are $(x_c, y_c, z_c, (t_- + t_+)/2)$, where (x_c, y_c, z_c) are the coordinates of the centroid of $\underline{S}$.

In addition to the above two types of hyperplanes, we shall also consider "hypercylinders" in E_4. A hypercylinder, denoted by $\Lambda(\underline{V}; t_-, t_+)$, is formed by all the points (x, y, z, t) that satisfy the conditions $(x, y, z) \in \underline{V}$ and $t_- \le t \le t_+$, where $\underline{V}$ is a 3D spatial region and t_- and t_+ $(t_- < t_+)$ are constants.

With the above preliminaries, $\mathrm{SE}(Q^*)$, the solution element of point Q^*—the point that lies on the nth time level and has $\underline{Q}^*$ as its spatial projection—is defined to be the union of $\Gamma(\underline{V}(24); t^n)$ and $\Gamma(\Delta(j); t^{n-1/2}, t^{n+1/2})$, $j = 1, 2, 3, \ldots, 12$, and their immediate neighborhoods. Moreover, the six BCEs of point Q, denoted by $\mathrm{CE}_\ell(Q)$, $\ell = 1, 2, \ldots, 6$, are defined to be the hypercylinders $\Lambda(\underline{V}(8; \ell); t^{n-1/2}, t^n)$, $\ell = 1, 2, \ldots, 6$, respectively. In addition, the CCE of point Q, denoted by $\mathrm{CE}(Q)$, is defined to be $\Lambda(\underline{V}(24); t^{n-1/2}, t^n)$, i.e., the union of the above six BCEs.

In this section, the set of the space-time mesh points whose spatial projections are the centroids of the hexahedrons that fill the 3D spatial computational domain is denoted by Ω and the set of the space-time mesh points whose spatial projections are the solution points of the centroids just referred to is denoted by Ω^*. Note that the BCEs and the CCE of any mesh point $\in \Omega$ and the SE of any mesh point $\in \Omega^*$ are defined in a manner identical to that described earlier for points Q and Q^*.

3.2. *Approximations within a Solution Element*

For any $Q^* \in \Omega^*$ and $(x, y, z, t) \in \text{SE}(Q^*)$, $u_m(x, y, z, t)$, $f_m(x, y, z, t)$, $g_m(x, y, z, t)$, $q_m(x, y, z, t)$, and $\mathbf{h}_m(x, y, z, t)$ are approximated by $u_m^*(x, y, z, t; Q^*)$, $f_m^*(x, y, z, t; Q^*)$, $g_m^*(x, y, z, t; Q^*)$, $q_m^*(x, y, z, t; Q^*)$, and $\mathbf{h}_m^*(x, y, z, t; Q^*)$, respectively (see below). For any $m = 1, 2, 3, 4, 5$, let

$$\begin{aligned} u_m^*(x, y, z, t; Q^*) &\stackrel{\text{def}}{=} (u_m)_{Q^*} + (u_{mx})_{Q^*}(x - x_{Q^*}) + (u_{my})_{Q^*}(y - y_{Q^*}) \\ &\quad + (u_{mz})_{Q^*}(z - z_{Q^*}) + (u_{mt})_{Q^*}(t - t^n), \end{aligned} \tag{3.8}$$

$$\begin{aligned} f_m^*(x, y, z, t; Q^*) &\stackrel{\text{def}}{=} (f_m)_{Q^*} + (f_{mx})_{Q^*}(x - x_{Q^*}) + (f_{my})_{Q^*}(y - y_{Q^*}) \\ &\quad + (f_{mz})_{Q^*}(z - z_{Q^*}) + (f_{mt})_{Q^*}(t - t^n), \end{aligned} \tag{3.9}$$

$$\begin{aligned} g_m^*(x, y, z, t; Q^*) &\stackrel{\text{def}}{=} (g_m)_{Q^*} + (g_{mx})_{Q^*}(x - x_{Q^*}) + (g_{my})_{Q^*}(y - y_{Q^*}) \\ &\quad + (g_{mz})_{Q^*}(z - z_{Q^*}) + (g_{mt})_{Q^*}(t - t^n), \end{aligned} \tag{3.10}$$

$$\begin{aligned} q_m^*(x, y, z, t; Q^*) &\stackrel{\text{def}}{=} (q_m)_{Q^*} + (q_{mx})_{Q^*}(x - x_{Q^*}) + (q_{my})_{Q^*}(y - y_{Q^*}) \\ &\quad + (q_{mz})_{Q^*}(z - z_{Q^*}) + (q_{mt})_{Q^*}(t - t^n), \end{aligned} \tag{3.11}$$

and

$$\begin{aligned} \mathbf{h}_m^*(x, y, z, t; Q^*) &\stackrel{\text{def}}{=} (f_m^*(x, y, z, t; Q^*), \quad g_m^*(x, y, z, t; Q^*), \\ &\quad q_m^*(x, y, z, t; Q^*), \quad u_m^*(x, y, z, t; Q^*)) \end{aligned} \tag{3.12}$$

be the 3D extension of Eqs. (2.4) and (2.7)–(2.9). Note that, in this section it is implicitly assumed that any notation that has a similar 2D version is defined similarly. The definition of such a notation will not be given explicitly here unless confusion could occur.

Moreover, we assume that, for any $(x, y, z, t) \in \text{SE}(Q^*)$, and any $m = 1, 2, 3, 4, 5$,

$$\frac{\partial u_m^*(x, y, t; Q^*)}{\partial t} + \frac{\partial f_m^*(x, y, t; Q^*)}{\partial x} + \frac{\partial g_m^*(x, y, t; Q^*)}{\partial y} + \frac{\partial q_m^*(x, y, t; Q^*)}{\partial z} = 0. \tag{3.13}$$

Thus, for any $m = 1, 2, 3, 4, 5$,

$$\begin{aligned} (u_{mt})Q^* &= -(f_{mx})_{Q^*} - (g_{my})_{Q^*} - (q_{mz})_{Q^*} \\ &= -\sum_{\ell=1}^{5} [(f_{m,\ell})_{Q^*}(u_{\ell x})_{Q^*} + (g_{m,\ell})_{Q^*}(u_{\ell y})_{Q^*} + (q_{m,\ell})_{Q^*}(u_{\ell z})_{Q^*}]. \end{aligned} \tag{3.14}$$

Using the equations given above, it can be shown that, *for the current 3D case, the only independent discrete variables associated with the space-time solution point* Q^* *are* $(u_m)_{Q^*}$, $(u_{mx})_{Q^*}$, $(u_{my})_{Q^*}$, *and* $(u_{mz})_{Q^*}$, $m = 1, 2, 3, 4, 5$.

3.3. *Evaluation of* $(u_m)_{Q^*}$

We begin with the following preliminaries:

(a) The boundary of $\text{CE}(Q)$ is formed by the "top face" $\Gamma(\underline{V}(24); t^n)$, the "bottom face" $\Gamma(\underline{V}(24); t^{n-1/2})$, and the 24 "side faces" $\Gamma(\Delta(k, \ell); t^{n-1/2}, t^n)$, $k = 1, 2, 3, 4$ and

$\ell = 1, 2, \ldots, 6$. Because $\underline{V}(24)$ is the union of $\underline{V}(8; \ell)$, $\ell = 1, 2, \ldots, 6$, the top (bottom) face is the union of $\Gamma(\underline{V}(8; \ell); t^n)$ ($\Gamma(\underline{V}(8; \ell); t^{n-1/2})$), $\ell = 1, 2, \ldots, 6$. From the above observations, one concludes that the boundary of $\mathrm{CE}(Q)$ belongs to the union of $\mathrm{SE}(Q^*)$ and $\mathrm{SE}(A'^*_\ell)$, $\ell = 1, 2, \ldots, 6$. Specifically, $\Gamma(\underline{V}(24); t^n)$ belongs to $\mathrm{SE}(Q^*)$, and for each $\ell = 1, 2, \ldots, 6$, $\Gamma(\underline{V}(8; \ell); t^{n-1/2})$ and $\Gamma(\Delta(k, \ell); t^{n-1/2}, t^n)$, $k = 1, 2, 3, 4$, belong to $\mathrm{SE}(A'^*_\ell)$. Note that $\Gamma(\underline{V}(8; \ell); t^n)$, $\ell = 1, 2, \ldots, 6$, the union of which is $\Gamma(\underline{V}(24); t^n)$, also belong to $\mathrm{SE}(A^*_\ell)$, $\ell = 1, 2, \ldots, 6$, respectively, and that $\Gamma(\underline{V}(24); t^{n-1/2})$, which is the union of $\Gamma(\underline{V}(8; \ell); t^{n-1/2})$, $\ell = 1, 2, \ldots, 6$, also belongs to $\mathrm{SE}(Q'^*)$. *However, in the evaluation of Eq.* (3.16) (*see below*), *by assumption,* $\Gamma(\underline{V}(24); t^n)$ *is considered to be a subset of* $SE(Q^*)$ *while* $\Gamma(\underline{V}(24); t^{n-1/2})$ *is considered to be the union of subsets of* $SE(A'^*_\ell)$, $\ell = 1, 2, \ldots, 6$.

(b) Let Γ be a hyperplane segment lying within $\mathrm{SE}(Q^*)$. Let A be the area of Γ, (x_c, y_c, z_c, t_c) be the coordinates of the centroid of Γ, and $\mathbf{n}$ be a unit vector normal to Γ. Then it can be shown that

$$\int_\Gamma \mathbf{h}^*_m \cdot d\mathbf{s} = \mathbf{h}^*_m(x_c, y_c, z_c, t_c; Q^*) \cdot A\mathbf{n}, \tag{3.15}$$

where $d\mathbf{s} = d\sigma\, \mathbf{n}$ with $d\sigma$ being the area of a surface element on Γ.

(c) Let V denote the volume of $\underline{V}(24)$, i.e., the area of the top face $\Gamma(\underline{V}(24); t^n)$ of $\mathrm{CE}(Q)$ (see comments (a)–(c) given following Eq. (3.5)). Because the unit outward normal vector (outward from the interior of $\mathrm{CE}(Q)$) of this face is $(0, 0, 0, 1)$, its surface vector (i.e., the unit outward normal vector multiplied by the area) is $(0, 0, 0, V)$.

(d) Let V^ℓ and (x^ℓ, y^ℓ, z^ℓ), respectively, denote the volume and the spatial coordinates of the centroid of any $\underline{V}(8; \ell)$. Then the surface vector, and the coordinates of the centroid of $\Gamma(\underline{V}(8; \ell); t^{n-1/2})$, respectively, are $(0, 0, 0, -V^\ell)$ and $(x^\ell, y^\ell, z^\ell, t^{n-1/2})$.

(e) Let S^ℓ_k, $(n^\ell_{kx}, n^\ell_{ky}, n^\ell_{kz})$, and $(x^\ell_k, y^\ell_k, z^\ell_k)$, respectively, denote the area, the spatial unit outward normal, and the coordinates of the centroid of any $\Delta(k, \ell)$. Then the surface vector, and the coordinates of the centroid of the side face $\Gamma(\Delta(k, \ell); t^{n-1/2}; t^n)$, respectively, are $(\Delta t/2)S^\ell_k(n^\ell_{kx}, n^\ell_{ky}, n^\ell_{kz}, 0)$ and $(x^\ell_k, y^\ell_k, z^\ell_k, t^n - \Delta t/4)$ (see comments (a)–(c) given following Eq. (3.6)).

(f) Note that: (i) $(x_{Q^*}, y_{Q^*}, z_{Q^*}, t^n)$ are the coordinates of the centroid Q^* of the top face $\Gamma(\underline{V}(24), t^n)$ of $\mathrm{CE}(Q)$; (ii) $u^*_m(x_{Q^*}, y_{Q^*}, z_{Q^*}, t^n; Q^*) = (u_m)_{Q^*}$ (see Eq. (3.8)); and (iii) the surface vector of the top face is $(0, 0, 0, V)$. As a result, Eq. (3.12) and (3.15) imply that the flux of $\mathbf{h}^*_m$ leaving $\mathrm{CE}(Q)$ through its top face is $(u_m)_{Q^*}V$. Similarly, by using the information presented in items (a), (b), (d), and (e), the flux of $\mathbf{h}^*_m$ leaving the other faces of $\mathrm{CE}(Q)$ can be evaluated in terms of the independent marching variables at points A'^*_ℓ, $\ell = 1, 2, 3, 4, 5, 6$.

Let

$$\oint_{S(CE(Q))} \mathbf{h}^*_m \cdot d\mathbf{s} = 0, \quad m = 1, 2, 3, 4, 5; \tag{3.16}$$

i.e., the total flux of $\mathbf{h}^*_m$ leaving $\mathrm{CE}(Q)$ through its boundary vanishes. Then, with the aid of the above preliminaries, it can be shown that

$$(u_m)_{Q^*} = \left(\sum_{\ell=1}^{6} R^\ell_m\right) \Big/ V, \quad m = 1, 2, 3, 4, 5, \tag{3.17}$$

where, for any $m = 1, 2, 3, 4, 5$ and any $\ell = 1, 2, \ldots, 6$,

$$R_m^\ell = V^\ell\, u_m^*\big(x^\ell, y^\ell, z^\ell, t^{n-1/2}; A_\ell'^*\big) - \sum_{k=1}^{4} \frac{\Delta t}{2} S_k^\ell \big[n_{kx}^\ell\ f_m^*\big(x_k^\ell, y_k^\ell, z_k^\ell, t^n - \Delta t/4; A_\ell'^*\big) + n_{ky}^\ell\, g_m^*\big(x_k^\ell, y_k^\ell, z_k^\ell, t^n - \Delta t/4; A_\ell'^*\big) + n_{kz}^\ell\, q_m^*\big(x_k^\ell, y_k^\ell, z_k^\ell, t^n - \Delta t/4; A_\ell'^*\big)\big]. \quad (3.18)$$

Here $u_m^*(x, y, z, t; A_\ell'^*)$, $f_m^*(x, y, z, t; A_\ell'^*)$, $g_m^*(x, y, z, t; A_\ell'^*)$, and $q_m^*(x, y, z, t; A_\ell'^*)$ are defined using Eqs. (3.8)–(3.11), respectively, with the understanding that the symbols Q^* and t^n in these equations be replaced by $A_\ell'^*$ and $t^{n-1/2}$, respectively. As a result, each R_m^ℓ and therefore each $(u_m)_{Q^*}$, an independent marching variable at the nth time level, is a function of several independent marching variables at the $(n - 1/2)$th time level, i.e., $(u_m)_{A_\ell'^*}$, $(u_{mx})_{A_\ell'^*}$, $(u_{my})_{A_\ell'^*}$, and $(u_{mz})_{A_\ell'^*}$, $m = 1, 2, 3, 4, 5$ and $\ell = 1, 2, \ldots, 6$.

3.4. *Evaluation of* $(u_{mx})_{Q^*}$, $(u_{my})_{Q^*}$, *and* $(u_{mz})_{Q^*}$

First, we perform a spatial translation of the polyhedron $A_1^*A_2^*A_3^*A_4^*A_5^*A_6^*$ so that the centroid of the resulting new polyhedron $A_1^oA_2^oA_3^oA_4^oA_5^oA_6^o$ coincides with Q^*. Let the centroid of the polyhedron $A_1^*A_2^*A_3^*A_4^*A_5^*A_6^*$ and its spatial coordinates be denoted by A^* and $(x_{A^*}, y_{A^*}, z_{A^*})$, respectively, and let $\delta x = x_{Q^*} - x_{A^*}$, $\delta y = y_{Q^*} - y_{A^*}$, and $\delta z = z_{Q^*} - z_{A^*}$. Then $(x_{A_\ell^o}, y_{A_\ell^o}, z_{A_\ell^o})$, the spatial coordinates of A_ℓ^o, $\ell = 1, 2, \ldots, 6$, are given by

$$x_{A_\ell^o} = x_{A_\ell^*} + \delta x, \quad y_{A_\ell^o} = y_{A_\ell^*} + \delta y, \quad \text{and} \quad z_{A_\ell^o} = z_{A_\ell^*} + \delta z. \quad (3.19)$$

As a preliminary for the following discussions, for $m = 1, 2, 3, 4, 5$ and $\ell = 1, 2, \ldots, 6$, let

$$(u_m)_{A_\ell^o} \stackrel{\text{def}}{=} u_m^*\big(x_{A_\ell^o}, y_{A_\ell^o}, z_{A_\ell^o}, t^n; A_\ell'^*\big), \quad (3.20)$$

$$\delta u_m^\ell \stackrel{\text{def}}{=} (u_m)_{A_\ell^o} - (u_m)_{Q^*}, \quad (3.21)$$

and

$$\delta x_\ell \stackrel{\text{def}}{=} x_{A_\ell^o} - x_{Q^*}, \quad \delta y_\ell \stackrel{\text{def}}{=} y_{A_\ell^o} - y_{Q^*}, \quad \delta z_\ell \stackrel{\text{def}}{=} z_{A_\ell^o} - z_{Q^*}. \quad (3.22)$$

Next consider the vertex $\underline{B}_1$ depicted in Fig. 5. This vertex is the common vertex of the central hexahedron and three of its neighbors. As an example, let the identification indices ℓ of these three neighbors be 1, 2, and 3. Then, for any $m = 1, 2, 3, 4, 5$, consider the four points in the x–y–z–u space with the coordinates $(x_{Q^*}, y_{Q^*}, z_{Q^*}, (u_m)_{Q^*})$ and $(x_{A_\ell^o}, y_{A_\ell^o}, z_{A_\ell^o}, (u_m)_{A_\ell^o})$, $\ell = 1, 2, 3$. It can be shown that the values of $\partial u/\partial x$, $\partial u/\partial y$, and $\partial u/\partial z$ on the hyperplane that intercepts the above four points are given by

$$\big(u_{mx}^{(1)}\big)_{Q^*} \stackrel{\text{def}}{=} \Delta_x/\Delta, \quad \big(u_{my}^{(1)}\big)_{Q^*} \stackrel{\text{def}}{=} \Delta_y/\Delta, \quad \big(u_{mz}^{(1)}\big)_{Q^*} \stackrel{\text{def}}{=} \Delta_z/\Delta \quad (\Delta \neq 0), \quad (3.23)$$

where

$$\Delta \stackrel{\text{def}}{=} \begin{vmatrix} \delta x_1 & \delta y_1 & \delta z_1 \\ \delta x_2 & \delta y_2 & \delta z_2 \\ \delta x_3 & \delta y_3 & \delta z_3 \end{vmatrix} \quad (3.24)$$

and

$$\Delta_x \overset{\text{def}}{=} \begin{vmatrix} \delta u_m^1 & \delta y_1 & \delta z_1 \\ \delta u_m^2 & \delta y_2 & \delta z_2 \\ \delta u_m^3 & \delta y_3 & \delta z_3 \end{vmatrix}, \quad \Delta_y \overset{\text{def}}{=} \begin{vmatrix} \delta x_1 & \delta u_m^1 & \delta z_1 \\ \delta x_2 & \delta u_m^2 & \delta z_2 \\ \delta x_3 & \delta u_m^3 & \delta z_3 \end{vmatrix}, \quad \Delta_z \overset{\text{def}}{=} \begin{vmatrix} \delta x_1 & \delta y_1 & \delta u_m^1 \\ \delta x_2 & \delta y_2 & \delta u_m^2 \\ \delta x_3 & \delta y_3 & \delta u_m^3 \end{vmatrix}. \tag{3.25}$$

Note that $\Delta = 0$ if and only if the spatial projections of A_1^o, A_2^o, A_3^o, and Q^* are coplanar and that for each $k = 2, 3, \ldots, 8$, $(u_{mx}^{(k)})_{Q^*}$, $(u_{my}^{(k)})_{Q^*}$, and $(u_{mz}^{(k)})_{Q^*}$ are defined by the above definition procedure except that $\underline{B}_1$ is replaced by $\underline{B}_k$.

With the above preliminaries, for each $m = 1, 2, 3, 4, 5$, $(u_{mx})_{Q^*}$, $(u_{my})_{Q^*}$, and $(u_{mz})_{Q^*}$ may be evaluated by

$$(u_{mx})_{Q^*} = \frac{1}{8}\sum_{k=1}^{8} \left(u_{mx}^{(k)}\right)_{Q^*}, \quad (u_{my})_{Q^*} = \frac{1}{8}\sum_{k=1}^{8} \left(u_{my}^{(k)}\right)_{Q^*}, \quad (u_{mz})_{Q^*} = \frac{1}{8}\sum_{k=1}^{8} \left(u_{mz}^{(k)}\right)_{Q^*}. \tag{3.26}$$

Alternatively, for a flow with steep gradients or discontinuities, the simple averages in Eq. (3.26) may be replaced by weighted averages, i.e.,

$$(u_{mx})_{Q^*} = \begin{cases} 0, & \text{if } \theta_{mk} = 0,\ k = 1, 2, \ldots, 8, \\ \sum_{k=1}^{8} \left[\left(W_m^{(k)}\right)^{\alpha} \left(u_{mx}^{(k)}\right)_{Q^*}\right] \Big/ \sum_{k=1}^{8} \left(W_m^{(k)}\right)^{\alpha}, & \text{otherwise,} \end{cases} \tag{3.27a}$$

$$(u_{my})_{Q^*} = \begin{cases} 0, & \text{if } \theta_{mk} = 0,\ k = 1, 2, \ldots, 8, \\ \sum_{k=1}^{8} \left[\left(W_m^{(k)}\right)^{\alpha} \left(u_{my}^{(k)}\right)_{Q^*}\right] \Big/ \sum_{k=1}^{8} \left(W_m^{(k)}\right)^{\alpha}, & \text{otherwise,} \end{cases} \tag{3.27b}$$

and

$$(u_{mz})_{Q^*} = \begin{cases} 0, & \text{if } \theta_{mk} = 0,\ k = 1, 2, \ldots, 8, \\ \sum_{k=1}^{8} \left[\left(W_m^{(k)}\right)^{\alpha} \left(u_{mz}^{(k)}\right)_{Q^*}\right] \Big/ \sum_{k=1}^{8} \left(W_m^{(k)}\right)^{\alpha}, & \text{otherwise.} \end{cases} \tag{3.27c}$$

Here $\alpha \geq 0$ is an adjustable constant (usually $\alpha = 1$ or $\alpha = 2$),

$$\theta_{mk} \overset{\text{def}}{=} \sqrt{\left[\left(u_{mx}^{(k)}\right)_{Q^*}\right]^2 + \left[\left(u_{my}^{(k)}\right)_{Q^*}\right]^2 + \left[\left(u_{mz}^{(k)}\right)_{Q^*}\right]^2}, \tag{3.28}$$

and for each k, $W_m^{(k)}$ is the product of $\theta_{m1}, \theta_{m2}, \ldots, \theta_{m8}$ *excluding* θ_{mk}. Note that: (i) to avoid dividing by zero, in practice a small positive number such as 10^{-60} is added to the denominators that appear in Eqs. (3.27a)–(3.27c); and (ii) Eqs. (3.27a)–(3.27c) reduce to Eq. (3.26) if $\alpha = 0$.

3.5. *Remarks and Discussions*

The present 3D Euler solver is formed using Eqs. (3.17) and (3.27a)–(3.27c). With some trivial modifications, most of the discussions about the 2D scheme given in Section 2.5 and the Appendix are also applicable to the present 3D scheme. In particular, the concept of local and global flux conservation can also be established for the present 3D scheme by using a redefinition procedure similar to that presented in the Appendix.

4. NUMERICAL RESULTS

The capabilities of the present 2D and 3D schemes are now demonstrated using three numerical examples.

4.1. *Shock Reflection on a Flat Plate*

This steady-state test problem was proposed by Yee *et al*. [28]. By imposing suitable upstream conditions, oblique incident and reflected shocks will appear above a flat plate. The spatial computational domain is a 4.0×1.0 rectangle containing 19,200 uniform rectangles. For the resulting space-time mesh, $\Omega^* = \Omega$ and Ω^* can be divided into two disjoint sets Ω^*_+ and Ω^*_- (see Section 2.5).

The flow conditions at $t = 0$ are [9]

$$(u, v, \rho, p) = \begin{cases} (2.9, 0.0, 1.0, 0.71428), & \text{ahead of the incident shock,} \\ (2.6193, -0.50632, 1.7, 1.5282), & \text{behind the incident shock,} \end{cases} \tag{4.1}$$

where u, v, ρ, and p, are x-velocity, y-velocity, mass density, and static pressure, respectively. For $t > 0$, (i) the flow conditions given in the first and second rows on the right side of Eq. (4.1) are imposed on the left and the top boundaries, respectively; (ii) the reflecting boundary conditions (see the bottom half of p. 124 in [9]) are imposed on the bottom boundary (a solid wall); and (iii) the nonreflecting conditions [9, 13] are imposed on the right boundary (a supersonic outlet).

Note that, for the reflecting boundary conditions used here, no mesh point lies on the solid wall. In addition, for each interior mesh point immediately neighboring to the solid wall, at the same time level there is a mirror image ghost mesh point lying just below the wall. Because the solution values at the ghost point are assigned to be the mirror-image values of its corresponding interior mesh point, and because one of the above two points belongs to Ω^*_+ while the other belongs to Ω^*_-, the solution values of Ω^*_+ and Ω^*_- are coupled by the present reflecting boundary conditions. In spite of this disadvantage, as explained in [9], the set of reflecting boundary conditions used here (which are also used in the following numerical examples) is the most robust among several sets of the reflecting boundary conditions described in [9]. Note that, because the marching over Ω^*_+ and that over Ω^*_- are completely decoupled from each other except for the mesh points immediately neighboring to the solid wall, only the solution values of one of Ω^*_+ and Ω^*_- are involved in producing Fig. 6b, although the numerical time-marching itself involves both Ω^*_+ and Ω^*_-. Here it should be emphasized that, for the current special problem in which only one straight solid wall is present, only one of Ω^*_+ and Ω^*_- needs to be used in the computation if, instead, one uses the reflecting boundary conditions similar to that described in [9, p. 122].

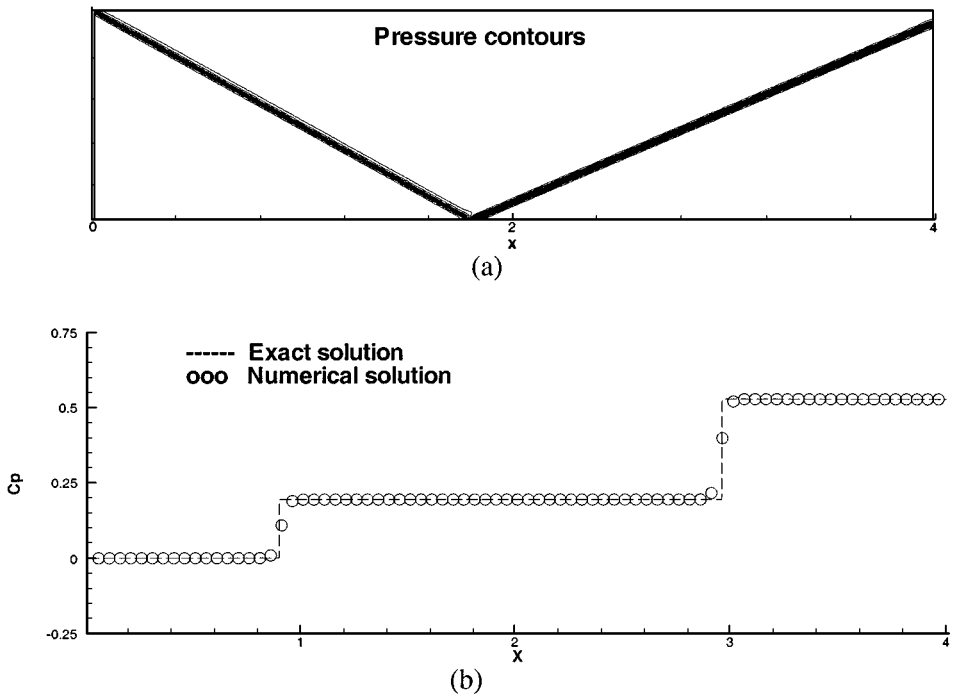

FIG. 6. The Euler solution of a steady-state shock reflection problem: (a) pressure contours; (b) pressure coefficient distribution at the mid-section of the computation domain ($y = 0.5$).

The pressure contours generated using the present 2D scheme with $\alpha = 2$ are shown in Fig. 6a. The angle between the computed reflected shock and the horizontal line is 23.28°, which is very close to the analytical value [27]. Furthermore, as shown in Fig. 6b, (i) the numerical values of the pressure coefficient at the horizontal mid-section of the rectangular domain agree very well with the analytical values; (ii) no numerical oscillations are detected near either the incident or the reflected shock; and (iii) both the incident and reflected shocks are resolved by a single data point.

4.2. *Shock Wave Diffraction over a Wedge*

This test problem, which was originally used by Wang [6], is based on a flow field given in the flow album edited by Van Dyke [29]. A planar shock wave at $M_s = 1.3$ moves toward a wedge with the angle $\theta = 26.565°$ (see Fig. 7a). Taking advantage of symmetry, only half of the flow field is simulated. The spatial computational domain is a rectangle with $-0.8 \le x \le 3.2$ and $0 \le y \le 1.1$, excluding the wedge. The whole domain is divided into 248, 750 nonuniform quadrilaterals and $\alpha = 1$ is assumed.

At $t = 0$, the incident planar shock is placed at $x = -0.5$. For $t > 0$, the constant behind-the-shock flow conditions are maintained at the left boundary, the reflecting boundary conditions are imposed on the upper and lower boundaries (note that the lower boundary is the symmetric center line), and also on the surfaces of the wedge, and the nonreflecting boundary conditions are imposed on the right boundary, a supersonic outlet.

To enhance the visual effect, the density countours of the entire flow field at three different times are presented in Figs. 7b–7d. When the planar shock reaches the wedge, a circular

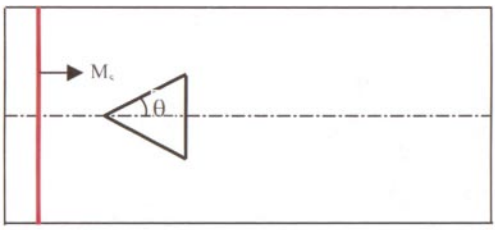

(a)

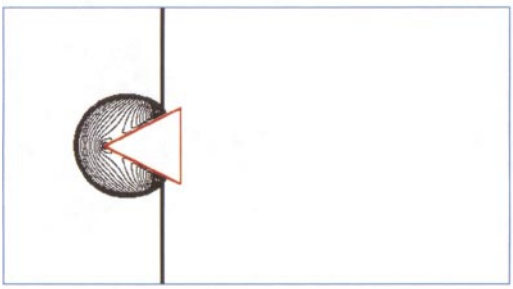

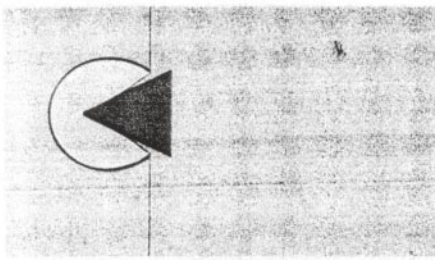

(b)

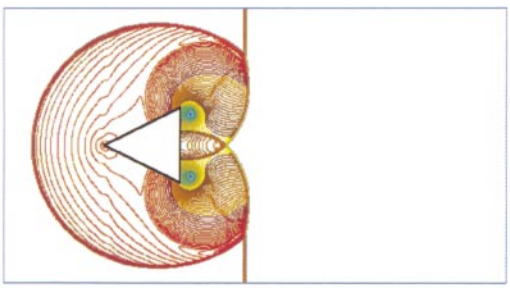

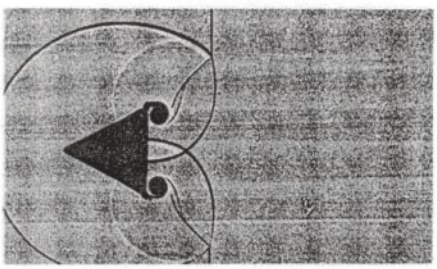

(c)

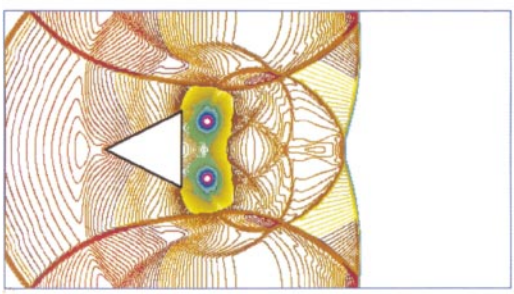

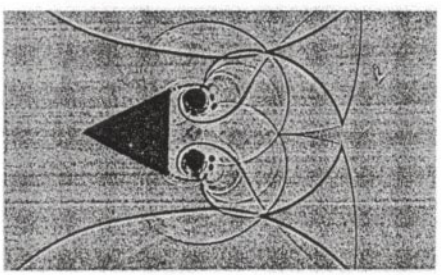

(d)

FIG. 7. Schematic (a) and density contours at three different times compared with the experimental photographs: (b) $t = 0.725$; (c) $t = 1.2125$; (d) $t = 1.825$.

reflection wave is generated. As the shock passes the wedge, the flow separates and vortices are formed around the two sharp corners. Further interaction between shocks and vortices produces increasingly elaborate patterns of shock waves, slip lines, and vortices. These results agree well with the experimental result [29] except for those phenomena induced by the viscous effect. Here, it should be pointed out that the exact locations of the upper

and lower walls in the experiment are not given in [29] (we only know that these walls are actually above and below the top and bottom edges of the photograph, respectively). As a result, the spatial domain assumed in the current simulation (which is slightly larger than the photographic frame) is only an approximation of the actual physical domain.

4.3. *Three-Dimensional Detonation*

The 3D scheme described in Section 3 has been extended to become a solver for conservation laws with source terms. Previously, we have reported numerical simulations of 1D and 2D detonation waves by using the CE/SE method [25]. Those results have been validated by comparing them with analytical solutions and numerical solutions reported by other researchers. In the present paper, 3D simulation of a detonation wave is performed by solving the reacting Euler equations. The chemical reactions are modeled by single-step, irreversible, and finite-rate kinetics. Two chemical species are considered, i.e., the reactant and the product. The Euler equations and one species equation are solved simultaneously. With proper nondimensionalization, it can be shown that the defining parameters of this detonation wave are the overdriven factor f, the specific heat ratio γ, the activation energy E^+, and the heat release rate q. In the present simulation, $f = 1.6$, $\gamma = 1.2$, $E^+ = 50$, and $q = 50$ are assumed.

In the current simulation, $\alpha = 1$ is assumed. Also, the spatial computational domain, a $8 \times 8 \times 6$ rectangular box, is divided into 6.4 million hexahedrons. Reflecting boundary conditions are imposed on the four lateral wall boundaries. The fresh reactant travels from top to bottom and is consumed by the frame front. On the top surface, the incoming flow conditions are specified. On the bottom surface, a nonreflecting boundary condition is imposed. The coordinate system is chosen such that the frame front stays in the horizontal mid-section of the rectangular box.

A snapshot of temperature countours is shown in Fig. 8. The flow field is composed of the quiescent state of the reactant ahead of the shock, a flame zone with finite rate reaction, and the equilibrium state behind the reaction zone. Because of the cellular structure of the detonation, the flow field is very complex. The shock front is characterized by triple points

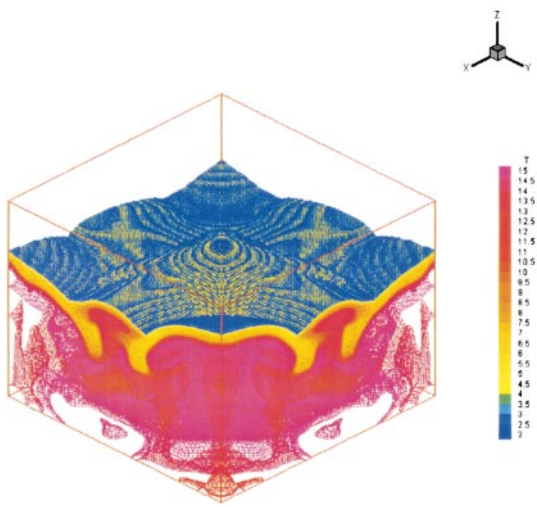

FIG. 8. Temperature contours for a simulated three-dimensional detonation wave in a square duct.

traveling in transverse directions. The colliding triple points create tremendous vortices. We observe the classical picture of "explosions within explosions" sustained by the propagating triple points at the detonation front. It is seen that a high-temperature region exists around triple points. At each collision of triple points, vortices with opposite signs are created and propagated downstream. Due to these vortices, unburnt reactant is pushed into the flame zone. The continuous burning of the pockets of the unburnt reactant behind the flame zone greatly extends the effective flame zone.

5. CONCLUDING REMARKS

In this paper, the original 2D and 3D CE/SE Euler a–α schemes (which use triangular and tetrahedral meshes, respectively) were extended to solve the 2D and 3D unsteady Euler equations using quadrilateral and hexahedral meshes, respectively. It has been shown that the present schemes retain many key advantages of other CE/SE schemes, i.e., efficient parallel computing, ease of implementing nonreflecting boundary conditions, high-fidelity solutions, and a genuinely multidimensional formulation without the need to use Riemann solvers. The only key disadvantage of the present schemes (and, for that matter, any other a–α scheme) is that, compared with other more general CE/SE schemes such as the a–ϵ–α–β schemes [9], they allow for less freedom in adjusting numerical dissipation. As explained in [9, Section 5.5], this inflexibility may impose a constraint on the performance of the current schemes in numerical simulations involving highly nonuniform meshes.

In addition, it was pointed out that, by combining the techniques used to construct the present and earlier CE/SE solvers, one could easily develop 2D and 3D mixed mesh solvers. An advantage of using such a mixed mesh is that a geometrically complex spatial subdomain can be filled easily using triangles or tetrahedrons while a less complex subdomain, such as a near-wall region, can be filled using quadrilaterals or hexahedrons.

A rigorous discussion about the concept of local and global flux conservation as applied to the present 2D scheme using an unstructured mesh is given in the Appendix. As a part of this discussion, a post-marching procedure was introduced to handle a "solution decoupling" problem that may arise after a long marching involving many time steps. Without any exception, the discussions given in the Appendix can be extended to three dimensions easily.

APPENDIX

In this appendix, using a technique similar to that presented in [10], local and global flux conservation is established for the present 2D scheme using an unstructured mesh. Also a post-marching procedure is introduced to handle the "solution decoupling" problem referred to in comment (f) of Section 2.5.

Note that, for the case in which the mesh decoupling referred to in comments (c) and (d) of Section 2.5 does not occur, generally the space-time computational domain cannot be filled by the union of a combination of nonoverlapping CCEs. As a result, global flux conservation cannot be established by summing over a set of local conservation conditions such as Eq. (2.13). However, even in the nondecoupling case, the computational domain can still be filled by the union of a combination of nonoverlapping BCEs. As a result, through a process of flux redefinition to be shown, one can manage to preserve the concept

of local and global flux conservation over the BCEs and the union of any combination of them.

As a preliminary, first we introduce the following definitions (see Fig. 4b):

(a) For any $m, \ell = 1, 2, 3, 4$, let $F_m^\ell(Q^*)$ denote the flux of $\mathbf{h}_m^*$ leaving $\mathrm{CE}(Q)$ through the top face of $\mathrm{CE}_\ell(Q)$, assuming that this top face belongs to $\mathrm{SE}(Q^*)$. Note that the top faces of $\mathrm{CE}_\ell(Q)$, $\ell = 1, 2, 3, 4$, are the quadrilaterals $A_1B_1QB_4$, $A_2B_2QB_1$, $A_3B_3QB_2$, and $A_4B_4QB_3$, respectively.

(b) For any $m, \ell = 1, 2, 3, 4$, let $F_m^\ell(A_\ell'^*)$ denote the flux of $\mathbf{h}_m^*$ leaving $\mathrm{CE}(Q)$ through the bottom face of $\mathrm{CE}_\ell(Q)$, assuming that this bottom face belongs to $\mathrm{SE}(A_\ell'^*)$. Note that the bottom faces of $\mathrm{CE}_\ell(Q)$, $\ell = 1, 2, 3, 4$, are the quadrilaterals $A_1'B_1'Q'B_4'$, $A_2'B_2'Q'B_1'$, $A_3'B_3'Q'B_2'$, and $A_4'B_4'Q'B_3'$, respectively.

(c) For any $m, \ell = 1, 2, 3, 4$ and any $k = 1, 2$, let $F_m^{(k,\ell)}(A'^*)$ denote the flux of $\mathbf{h}_m^*$ leaving $\mathrm{CE}(Q)$ through its (k, ℓ) side face, assuming that this side face belongs to $\mathrm{SE}(A_\ell'^*)$. Note that the (k, ℓ) ($k = 1, 2$, $\ell = 1, 2, 3, 4$) side faces of $\mathrm{CE}(Q)$ are defined in Comments (e) of Section 2.3.

With the above definitions, local flux conservation over $\mathrm{CE}(Q)$, i.e., Eq. (2.13), implies that

$$\sum_{\ell=1}^{4} S_m^\ell(Q^*, A_\ell'^*) = 0, \tag{A.1}$$

where

$$S_m^\ell(Q^*, A_\ell'^*) \stackrel{\text{def}}{=} F_m^\ell(Q^*) + F_m^\ell(A_\ell'^*) + F_m^{(1,\ell)}(A_\ell'^*) + F_m^{(2,\ell)}(A_\ell'^*). \tag{A.2}$$

Note that Eq. (A.1) says nothing about local flux conservation over $\mathrm{CE}_\ell(Q)$, $\ell = 1, 2, 3, 4$. As is shown in the following, local flux conservation over these BCEs can be realized with a proper assignment of "artificial fluxes" over the four interfaces that divide $\mathrm{CE}(Q)$ into $\mathrm{CE}_\ell(Q)$, $\ell = 1, 2, 3, 4$.

To proceed, note that the boundary of each $\mathrm{CE}_\ell(Q)$ is formed by the top face, the bottom face, and the four side faces. Among these four side faces, two are also the side faces of $\mathrm{CE}(Q)$ while the other two belong to the set of the four interfaces that divide $\mathrm{CE}(Q)$ into $\mathrm{CE}_\ell(Q)$, $\ell = 1, 2, 3, 4$. Hereafter, the first pair and second pair of the above four side faces, respectively, are referred to as the "exterior" and "interior" side faces of $\mathrm{CE}_\ell(Q)$. Obviously, for each m, the four terms on the right side of Eq. (A.2) represent the fluxes leaving $\mathrm{CE}_\ell(Q)$ through its top face, bottom face, and two exterior side faces, respectively.

Next, for any $m = 1, 2, 3, 4$, let $F_m^{1:2}(Q)$ represent a flux (as yet to be defined explicitly) leaving $\mathrm{CE}_1(Q)$ (and entering $\mathrm{CE}_2(Q)$) through the interface dividing $\mathrm{CE}_1(Q)$ and $\mathrm{CE}_2(Q)$. $F_m^{2:3}(Q)$, $F_m^{3:4}(Q)$, and $F_m^{4:1}(Q)$ are similarly defined. In addition, for any $m = 1, 2, 3, 4$, let

$$S_m^1(Q^*, A_1'^*) + F_m^{1:2}(Q) - F_m^{4:1}(Q) = 0, \tag{A.3a}$$

$$S_m^2(Q^*, A_2'^*) + F_m^{2:3}(Q) - F_m^{1:2}(Q) = 0, \tag{A.3b}$$

$$S_m^3(Q^*, A_3'^*) + F_m^{3:4}(Q) - F_m^{2:3}(Q) = 0, \tag{A.3c}$$

$$S_m^4(Q^*, A_4'^*) + F_m^{4:1}(Q) - F_m^{3:4}(Q) = 0. \tag{A.3d}$$

Note that $S_m^1(Q^*, A_1'^*)$ represents the sum of the fluxes leaving $\mathrm{CE}_1(Q)$ through its top face, bottom face, and two exterior side faces and that $F_m^{1:2}(Q)$ and $-F_m^{4:1}(Q)$, respectively, represent the fluxes leaving $\mathrm{CE}_1(Q)$ through its two interior side faces. Thus, for each m, Eq. (A.3a) represents a local flux conservation relation over $\mathrm{CE}_1(Q)$. Similarily, for each m, Eqs. (A.3b)–(A.3d) represent local flux conservation relations over $\mathrm{CE}_2(Q)$, $\mathrm{CE}_3(Q)$, and $\mathrm{CE}_4(Q)$, respectively.

Note that a summation over Eqs. (A.3a)–(A.3d) results in Eq. (A.1)—the known local conservation condition over $\mathrm{CE}(Q)$. Thus, for each m, Eqs. (A.3a)–(A.3d) contain only three independent conditions for four unknowns $F_m^{1:2}(Q)$, $F_m^{2:3}(Q)$, $F_m^{3:4}(Q)$, and $F_m^{4:1}(Q)$. In other words, there still is a degree of freedom left for these unknowns.

To proceed, note that the interfaces that divide $\mathrm{CE}(Q)$ into $\mathrm{CE}_\ell(Q)$, $\ell = 1, 2, 3, 4$, all belong to $\mathrm{SE}(Q^*)$. As a result, even though they are not used in the construction of the present scheme, the fluxes of $\mathbf{h}_m^*$ at these interfaces can be evaluated in terms of the independent marching variables at point Q^*. In the following discussion, the evaluated flux of $\mathbf{h}_m^*$ leaving $\mathrm{CE}_1(Q)$ (and entering $\mathrm{CE}_2(Q)$) through the interface dividing $\mathrm{CE}_1(Q)$ and $\mathrm{CE}_2(Q)$ will be denoted by $F_m^{1:2}(Q^*)$. Similarily, one also define $F_m^{2:3}(Q^*)$, $F_m^{3:4}(Q^*)$, and $F_m^{4:1}(Q^*)$.

With the above definitions, the degree of freedom referred to earlier is removed by requiring that, for each m, $F_m^{1:2}(Q)$, $F_m^{2:3}(Q)$, $F_m^{3:4}(Q)$, and $F_m^{4:1}(Q)$ be the solution to Eqs. (A.3a)–(A.3d) with the minimal value of

$$L_m \stackrel{\text{def}}{=} \left[F_m^{1:2}(Q) - F_m^{1:2}(Q^*)\right]^2 + \left[F_m^{2:3}(Q) - F_m^{2:3}(Q^*)\right]^2 + \left[F_m^{3:4}(Q) - F_m^{3:4}(Q^*)\right]^2 + \left[F_m^{4:1}(Q) - F_m^{4:1}(Q^*)\right]^2. \tag{A.4}$$

It can be shown that the last requirement amounts to imposing the extra condition

$$F_m^{1:2}(Q) + F_m^{2:3}(Q) + F_m^{3:4}(Q) + F_m^{4:1}(Q) = F_m^{1:2}(Q^*) + F_m^{2:3}(Q^*) + F_m^{3:4}(Q^*) + F_m^{4:1}(Q^*). \tag{A.5}$$

By using Eq. (A.5) and any three of Eqs. (A.3a)–(A.3d), for each m, $F_m^{1:2}(Q)$, $F_m^{2:3}(Q)$, $F_m^{3:4}(Q)$, and $F_m^{4:1}(Q)$ can be uniquely defined in terms of known parameters $F_m^{1:2}(Q^*)$, $F_m^{2:3}(Q^*)$, $F_m^{3:4}(Q^*)$, $F_m^{4:1}(Q^*)$, and $S_m^\ell(Q^*, A_\ell'^*)$, $\ell = 1, 2, 3, 4$.

Next, note that a space-time region may be the common BCE of two different mesh points (these two mesh points are referred to as the cohosts of the common BCE). As an example, the space-time cylinder $A_1B_1QB_4A_1'B_1'Q'B_4'$ depicted in Fig. 4b was designated as $\mathrm{CE}_1(Q)$. However, it also can be designated as a BCE of point A_1, say $\mathrm{CE}_1(A_1)$. As is shown in the following remarks, for each m, how the flux is assigned to each face of the space-time cylinder, along with the resulting flux conservation relation over the cylinder, depends on whether it is designated as $\mathrm{CE}_1(Q)$ or $\mathrm{CE}_1(A_1)$:

(a) At the top face of $\mathrm{CE}_1(Q)$ ($\mathrm{CE}_1(A_1)$), the flux is evaluated assuming that the face belongs to $\mathrm{SE}(Q^*)$ ($\mathrm{SE}(A_1^*)$).

(b) At the bottom face of $\mathrm{CE}_1(Q)$ ($\mathrm{CE}_1(A_1)$), the flux is evaluated assuming that the face belongs to $\mathrm{SE}(A_1'^*)$ ($\mathrm{SE}(Q'^*)$).

(c) The exterior (interior) side faces of $\mathrm{CE}_1(Q)$ are the interior (exterior) side faces of $\mathrm{CE}_1(A_1)$.

(d) At each of the exterior side faces of $\mathrm{CE}_1(Q)$ ($\mathrm{CE}_1(A_1)$), the flux is evaluated assuming that the side face belongs to $\mathrm{SE}(A_1'^*)$ ($\mathrm{SE}(Q^*)$).

(e) A local conservation condition over $\mathrm{CE}_1(A_1)$ (different from that over $\mathrm{CE}_1(Q)$, i.e., Eq. (A.3a)) will result if the artificial flux at each interior side face of $\mathrm{CE}_1(A_1)$ is also assigned using a procedure parallel to that used to assign the flux at each interior side face of $\mathrm{CE}_1(Q)$.

Consider a common BCE of two cohosts lying in the interior of the computational domain. From the above discussion, one concludes that, for each m, two different fluxes are assigned to each face of the BCE, and corresponding to the two cohosts, there are two different conservation relations over this BCE. Hereafter, *the simple average of the two fluxes at each face will be referred to as the generalized flux at this face*. By summing the two local conservation relations over the BCE, one concludes that the total generalized flux leaving the BCE through its boundary vanishes.

Furthermore, note that only one generalized flux is defined at any interface dividing two neighboring BCEs and that the generalized flux leaving a BCE through an interface dividing this BCE and a neighboring BCE is the negative of the generalized flux leaving the neighboring BCE through the same interface. Thus, one arrives at the following global flux conservation relation: *For each m, the total generalized flux leaving the boundary of any space-time region that is the union of any combination of BCEs (with each of these BCEs having two interior cohosts) vanishes*.

To proceed further, note that, for each m, corresponding to its two cohosts, the boundary of a BCE is assigned two sets of fluxes. Because of the space-time staggering nature of the stencil of the present scheme, the above two sets along with the solution values at its two cohosts may become decoupled locally after many marching steps. Note that one may argue that this decoupling does not matter, because the amount of decoupling usually is of the order of the discrepancy between the numerical solution and the exact solution and, as such, it does not exacerbate the actual simulation errors. However, in practice, the decoupling can cause a substantial problem in solution display. The decoupling can manifest itself as what appear to be small-wavelength oscillations when the solution at the final time level is displayed using the solution values of both Ω^*_+ and Ω^*_-. As is shown in the following paragraph, not only does the above definition of a unique generalized flux at any boundary of a BCE provide a way to avoid the problem of "flux decoupling," it also provides a way to handle the problem of "solution decoupling."

Consider the top face of any BCE with two cohosts. For any m, the two fluxes assigned to this face, respectively, are evaluated assuming that the face belongs to the SEs of its two cohosts, respectively. It can be shown that these two fluxes, respectively, are equal to the area of the face multiplied by the two values of u_m at the centroid of the top face evaluated assuming that the centroid belongs to the two cohosts, respectively. Let the simple average of the above two values of u_m be referred to as the *coupled* solution value of u_m at the centroid of the top face of this BCE. Then it can easily be shown that, for each m, the generalized flux at this face is simply the area of the face multiplied by the new solution value. Also, because of how these new solution values are defined, solution decoupling generally is no longer a problem if the numerical data are taken from these new solution values.

Finally, it should be emphasized that the above definition of generalized fluxes and coupled solution values by no means implies any change in the marching scheme. In fact, evaluation of the locations of the centroids of the top faces of the BCEs along with that of the associated coupled solution values represents only a post-marching procedure.

REFERENCES

1. S. C. Chang and W. M. To, *A New Numerical Framework for Solving Conservation Laws—The Method of Space-Time Conservation Element and Solution Element*, NASA TM 104495 (NASA, August 1991).
2. S. C. Chang and W. M. To, A brief description of a new numerical framework for solving conservation laws—The method of space-time conservation element and solution element, in *Proceedings of the Thirteenth International Conference on Numerical Methods in Fluid Dynamics, Rome, Italy, 1992*, edited by M. Napolitano and F. Sabetta, Lecture Notes in Physics 414 (Springer-Verlag, New York/Berlin, 1992), p. 396.
3. S. C. Chang, *New Developments in the Method of Space-Time Conservation Element and Solution Element—Applications to the Euler and Navier–Stokes Equations*, NASA TM 106226 (NASA, August 1993).
4. S. C. Chang, X. Y. Wang, and C. Y. Chow, *New Developments in the Method of Space-Time Conservation Element and Solution Element—Applications to Two-Dimensional Time-Marching Problems*, NASA TM 106758 (NASA, December 1994).
5. S. C. Chang, The method of space-time conservation element and solution element—A new approach for solving the Navier–Stokes and Euler equations, *J. Comput. Phys.* **119**, 295 (1995).
6. X. Y. Wang, *Computational Fluid Dynamics Based on the Method of Space-Time Conservation Element and Solution Element*, Ph.D. dissertation, (Department of Aerospace Engineering, University of Colorado, Boulder, 1995).
7. S. C. Chang, S. T. Yu, A. Himansu, X. Y. Wang, C. Y. Chow, and C. Y. Loh, The method of space-time conservation element and solution element—A new paradigm for numerical solution of conservation laws, in *Computational Fluid Dynamics Review 1998*, edited by M. M. Hafez and K. Oshima (World Scientific, Singapore), Vol. 1, p. 206.
8. S. C. Chang, X. Y. Wang, and C. Y. Chow, *The Space-Time Conservation Element and Solution Element Method—A New High-Resolution and Genuinely Multidimensional Paradigm for Solving Conservation Laws. I. The Two-Dimensional Time Marching Schemes*, NASA TM 208843 (NASA, December 1998).
9. S. C. Chang, X. Y. Wang, and C. Y. Chow, The space-time conservation element and solution element method: A new high-resolution and genuinely multidimensional paradigm for solving conservation laws, *J. Comput. Phys.* **156**, 89 (1999).
10. X. Y. Wang and S. C. Chang, A 2D non-splitting unstructured triangular mesh Euler solver based on the space-time conservation element and solution element method, *Comput. Fluid Dyn. J.* **8**(2), 309 (1999).
11. X. Y. Wang and S. C. Chang, *A 3D Structured/Unstructured Euler Solver Based on the Space-Time Conservation Element and Solution Element Method*, Technical Paper 3278 (AIAA Press, Washington DC, 1999).
12. S. C. Chang, X. Y. Wang, and W. M. To, Application of the space-time conservation element and solution element method to one-dimensional convection-diffusion problems, *J. Comput. Phys.* **165**, 189 (2000).
13. S. C. Chang, A. Himansu, C. Y. Loh, X. Y. Wang, S. T. Yu, and P. Jorgenson, *Robust and Simple Non-Reflecting Boundary Conditions for the Space-Time Conservation Element and Solution Element Method*, Technical Paper 2077 (AIAA Press, Washington, DC, 1997).
14. N. S. Liu and K. H. Chen, Flux: an alternative flow solver for the National Combustion Code, AIAA Paper 99-1079 (1999).
15. C. Y. Loh, L. S. Hultgren, and S. C. Chang, Wave computation in compressible flow using the space-time conservation element and solution element method, *AIAA J.* **39**(5), 794 (2001).
16. C. Y. Loh, L. S. Hultgren, S. C. Chang, and P. C. E. Jorgenson, *Noise Computation of a Supersonic Shock-Containing Axisymmetric Jet by the CE/SE Method*, AIAA Technical Paper 0475 (AIAA Press, Washington, DC, 2000).
17. C. Y. Loh, L. S. Hultgren, and P. C. E. Jorgenson, *Near Field Screech Noise Computation for an Underexpanded Supersonic Jet by the CE/SE Method*, AIAA Technical Paper 2252 (AIAA Press, Washington, DC, 2001).
18. Z. C. Zhang and M. Y. Shen, New approach to obtain space-time conservation scheme, *Chin. J. Aeronaut*, **10**, 87 (1997).
19. Z. C. Zhang and M. Y. Shen, Improved scheme of space-time conservation element and solution element, *J. Tsinghua Univ. (Sci. & Tech.)* **37**, 65 (1997) [in Chinese].

20. Z. C. Zhang, A new general space-time conservation scheme for 2D Eular equations, *Chin. J. Comput. Mech.* **14**, 377 (1997) [in Chinese].
21. Z. C. Zhang and M. Y. Shen, New space-time conservation schemes for solving 2D Eular equation, *Acta Mech. Sinica* **31**, 152 (1999) [in Chinese].
22. Z. C. Zhang and S. T. Yu, *Shock Capturing without Riemann Solver—A Modified Space-Time CE/SE Method for Conservation Laws*, AIAA Technical Paper 0904 (AIAA Press, Washington, DC, 1999).
23. Z. C. Zhang, S. T. Yu, and S. C. Chang, A. Himansu, and P. Jorgenson, *A Modified Space-time CE/SE Method for Euler and Navier–Stokes Equations*, AIAA Technical Paper 3277 (AIAA Press, Washington, DC, 1999).
24. G. Cook, *High Accuracy Capture of Curved Shock Front Using the Method of Conservation Element and Solution Element*, AIAA Technical Paper 1008 (AIAA Press, Washington, DC, 1999).
25. S. J. Park, S. T. Yu, and M. C. Lai, *Numerical Calculation of Unstable Detonations by the Method of Space-Time Conservation Element and Solution Element*, AIAA Technical Paper 0491 (AIAA Press, Washington, DC, 1999).
26. Z. C. Zhang and S. T. John Yu, *A Generalized Space-Time CE/SE Method for the Euler Equations on Quadrilateral and Hexagonal Meshes*, AIAA Technical Paper 2592 (AIAA Press, Washington, DC, 2001).
27. M. Vinokur, An analysis of finite-difference and finite-volume formulations of conervation laws, *J. Comput. Phys.* **81**, 1 (1989).
28. H. C. Yee, R. F. Warming, and A. Harten, *Implicit Total Variation Diminishing (TVD) Scheme for Steady-State Calculations*, AIAA Technical Paper 1902 (AIAA Press, Washington, DC, 1983).
29. M. Van Dyke, *An Album of Fluid Motion* (The parabolic Press, Stanford, CA, 1988).